Geomorphology 466 (2024) 109416

Contents lists available at ScienceDirect

Geomorphology

journal homepage: www.journals.elsevier.com/geomorphology

Multi-millennia surface dynamics: Novel investigation approach unveils climate relation to mountain erosion (Serra da Estrela, Portugal)

Gerald Raab [a,b,*], Gonçalo Vieira [c], Piotr Migoń [d], Dmitry Tikhomirov [b], Marcus Christl [e], Markus Egli [b], Fabio Scarciglia [f]

[a] Department of Earth and Environmental Sciences, Dalhousie University, PO BOX 15000, 1459 Oxford Street, Halifax, Canada
[b] Department of Geography, University of Zurich, Winterthurerstrasse 190, 8057 Zurich, Switzerland
[c] Centro de Estudos Geográficos, Associate Laboratory TERRA, IGOT, University of Lisbon, Rua Branca Edmée Marques, 1600-276 Lisbon, Portugal
[d] University of Wrocław, Institute of Geography and Regional Development, pl. Uniwersytecki 1, 50-137 Wrocław, Poland
[e] Department of Physics, ETH Zürich, Otto-Stern-Weg 5, 8093 Zürich, Switzerland
[f] Dipartimento di Biologia, Ecologia e Scienze della Terra (DiBEST), Università della Calabria, Via P. Bucci – Cubo 15B, 87036 Rende, (CS), Italy

ARTICLE INFO

Keywords:
Long-term denudation
Rock weathering
Tor
Iberian Peninsula
Terrestrial cosmogenic nuclides (TCN)
Last Glacial Maximum

ABSTRACT

Multi-millennia data logs on surface denudation variation in alpine landscapes are scarce, yet they are needed to understand the impacts of environmental changes on denudation. On the example of the Serra da Estrela plateau in Portugal, we explored a new archive, vertical bedrock outcrops (tors), and the capability of the Tor Exhumation/Exposure Approach (TEA) to capture surface denudation variations even in formerly glaciated landscapes. Therefore, we used vertical in-situ ^{10}Be to date surface exposure of tor slopes in formerly glaciated and non-glaciated parts of the plateau during the last glacial period.

Based on the surface exposure ages, surface denudation variations covering the last ~200 ka could be derived that revealed glacial retreat dynamics in greater detail. Higher isotope contents and, thus, surface exposure ages were found in the non-glaciated area. At the formerly glaciated sites, the ice margin retreat is reflected in the isotope signature of the tors. The younger rock surfaces had a higher chemical weathering degree than older surfaces at the non-glaciated site as a result of a higher water availability. Highest-elevation tors have experienced (subglacial/hydrothermal) chemical weathering, mass wasting and stripping (~6 ± 0.5 ka) during the transition from a cool moist, to an oceanic-Mediterranean climate.

Yet, tors in the non-glaciated area yielded lower surface denudation rates with a maximum of 0.53 [mm yr^{-1}] compared to the glaciated area (reaching values of up to 18.29 [mm yr^{-1}]). Since the LGM and the concomitant increase in air temperature, surface denudation also distinctly changed. Temperature trends and surface denudation developed analogously for the last ~150 ka. Vegetation change or human activity's impact on surface denudation cannot be discerned due to the too low chronological resolution. Overall, we demonstrated that multi-millennia tor records of variation in surface denudation can be obtained using the TEA, even in formerly glaciated areas. Thus, this study contributes to revealing the sensitivity of mountain erosion rates to past environmental changes.

1. Introduction

The recent increase in extreme weather events (e.g., droughts, heavy rainfall, floods) reminds us of the vulnerability of erodible landscapes. This is particularly true for countries with mountainous landscapes and steep slopes (e.g., Saunders and Young, 1983) since >50 % of the total global denudation occurs on the steepest terrestrial surface parts of Earth (Larsen et al., 2014). One major scientific challenge in determining terrain changes is to capture temporal variability of these physical denudation processes (e.g., Stock and Montgomery, 1999; Shuster et al., 2011; Valla et al., 2011). Particularly within the denudation zone (e.g., mountain ranges, upland plateaus), we face a methodological gap in quantifying erosion variations over multi-millennia time scales (Einsele and Hinderer, 1998; Schaller and Ehlers, 2006; Hinderer et al., 2013).

Current approaches base the historical logs of surface denudation

* Corresponding author at: Department of Earth and Environmental Sciences, Dalhousie University, PO BOX 15000, 1459 Oxford Street, Halifax, Canada.
E-mail address: gr.science@gmx.at (G. Raab).

https://doi.org/10.1016/j.geomorph.2024.109416
Received 28 February 2024; Received in revised form 18 August 2024; Accepted 1 September 2024
Available online 4 September 2024

variation usually on sediment yields (e.g., Kirchner et al., 2001), bedload fluxes (e.g., sediment gauging; Meade, 1988), or lake and marine sedimentation (e.g., Mourier et al., 2010). Although these methods provide insights into past variability of surface denudation, they represent more of the catchment area and do not accurately depict the processes at the denudation zone. In contrast, modern isotope techniques allow a direct determination of surface denudation rates in mountains. Basin-wide average rates derived from terrestrial cosmogenic nuclides (TCN) (e.g., Wittmann et al., 2015; Gonzalez et al., 2016) or fallout radionuclides (FRN) techniques (e.g., Wallbrink and Murray, 1993; Walling, 1998) enable for the quantification of long (10^3–10^6 years) and short-term (last ~60 years) denudation rates, respectively. Although these isotope-derived rates are gathered within the denudation zone, they only represent average rates and provide only little information on the variability over time. Thus, despite the pioneering work in understanding surface denudation in alpine environments (Schaller et al., 2001, 2010; Norton et al., 2010; Hall et al., 2012; or Heimsath et al., 2001a, 2001b, 2012), these current methods only allow for the determination of average erosion rates.

Limited Information about temporal changes in the efficacy of these processes hinders a comprehensive understanding of surface processes in general. Only capturing the full spatial and temporal variations of surface evolution will enable for a more holistic understanding of the underlying driving controls (e.g., climate, vegetation, tectonics, land use). To facilitate more accurate projections on the impact of environmental changes (e.g., due to climate variations), one must first fully understand the causes and effects of past fluctuations in surface denudation. Hence, a new investigation technique that determines surface denudation variations within the denudational zone and over geological time scales must be developed and tested.

Recently, a new archive could be used and it seems that it may help to better decipher landscape and surface changes. The approach uses large residual bedrock outcrops, so-called tors (Linton, 1955; Migoń, 2006; Ballantyne, 2018). Tors have a higher physical resistance than the surrounding area, typically underlain by a weathering mantle (saprolite) that is more easily erodible. Heimsath et al. (2001a) initiated using tors to derive in-situ landscape denudation changes. However, TCN techniques were still novel, and the method remained dormant for nearly two decades. The modern concept of a tor exhumation/exposure approach (TEA) was revived and redeveloped by Raab (2019) and has now been successfully tested in unglaciated uplands (Raab et al., 2018) as well as in plutonic (granitic) (Raab et al., 2019) and metasedimentary (schist) (Raab et al., 2021) tor landscapes.

The TEA derives rates and changes of rates of landscape lowering, thus surface denudation ($D_{Surface}$), over multi-millennia and within the investigated landscape, including the denudation zone. $D_{Surface}$ is defined by the sum of physical erosion (E) and the leaching of chemical weathering products (W):

$$D_{Surface} = E + W$$

The archived $D_{Surface}$ information is deciphered by using TCN surface dating techniques applied to tors, over which the rate of exposure (exhumation rate) of their surfaces is determined. The correlation of the extrapolated exposure ages and their variations with various controls of surface denudation (e.g., land-use changes, climate data) provides a better understanding of past and ongoing landscape-forming processes.

However, mountainous landscapes have often endured past glacial morphogenesis. This intense landscape (re-)shaping during Quaternary glaciations, but also non-glacial processes (Oliva et al., 2019), can potentially influence tor archives and their TCN signatures (Phillips et al., 2006; Hughes et al., 2022). This could hinder the broader applicability of the promising TEA. Depending on geographic location, geomorphology, atmospheric circulatios, the last glacial maximum (LGM) varied (27.5–23.3 ka BP after Hughes and Gibbard, 2015; 26.5 to 19 ka BP after Clark, 2009; some local glacier maxima occurred earlier, 30–32 ka BP, Oliva et al., 2019). However, depending on the local thermal conditions of the ice cover, the columnar tor structure can be preserved, and even isotopic signatures older than the LGM can survive, as past investigations revealed (e.g., Gunnell et al., 2013; Phillips et al., 2006). Thus, the hope of the TEA to become an applicable method for formerly glaciated areas prevails. Yet a systemic and comparative study on the applicability of the TEA in a formerly glaciated area is still required.

This study aims to compare the ^{10}Be isotope signatures of tors at two end-member sites (one previously glaciated, and the second one not glaciated during the last two glaciations) and to derive multi-millennia $D_{Surface}$ variations of the surrounding landscape within a formerly glaciated area (FGA) and non-glaciated area (NGA). Among the various tor-hosting landscape types worldwide, we considered upland plateaus the best framework for such comparative studies. Upland plateaus allow for a comparison of tors from an NGA and FGA, but with analogous environmental conditions. The Estrela UNESCO Global Geopark of the Serra da Estrela in Portugal ideally fulfilled this condition and has >600, many exceptionally well preserved, tors across its plateaus (Migoń and Vieira, 2014).

We started our investigation with six hypotheses: (i) The tor exhumation/exposure approach (TEA, Raab et al. (2018)) can be used to decipher $D_{Surface}$ of former glaciated areas; (ii) The isotope signatures between tors in glaciated and never glaciated areas differ, as glaciers caused rejuvenation of the rock surface; (iii) The timing of glacial retreat is reflected in exposure ages derived from tors in the formerly glaciated area; (iv) Rejuvenated/younger tor rock surface (particular from glaciated areas) have a lower degree of chemical weathering; (v) Higher $D_{Surface}$ is expected in formerly glaciated areas due to the increased erosion; and (vi) Higher erosion rates are expected to have occurred during transition periods (e.g., cold–warm phases or warm–cold phases).

The resulting data is compared to climate changes and other controlling factors (e.g., vegetation dynamics) to establish a time-trend model with surface responses. Our study intends to broaden the applicability of tor archives for reconstructing surface processes in the Holocene and Pleistocene. We anticipate obtaining detailed rates of past variability of landscape erosion during or after glacial periods that will contribute to better the understanding of past climate change's impact on the selected mountainous landscape.

2. Study area

2.1. The upland plateau

The Serra da Estrela is situated in the central north of Portugal and is part of the Iberian Central Cordillera (Fig. 1a). Two steep fault-generated escarpments constitute the boundaries of the mountain massif with a relative relief of over 1000 m (Vieira, 2008). The highest part of the Serra da Estrela is divided into two plateaus (Fig. 1b). The eastern plateau lies just below 1750 m a.s.l, while the western plateau has the highest elevation in the Portugal's mainland with an altitude of 1993 m a.s.l.). Lautensach (1929), Daveau (1971) and Vieira (2004, 2008) showed that during the LGM the western plateau area was covered by a plateau icefield from which several valley glaciers radiated in various directions (Fig. 1b). In contrast, on the eastern plateau only a small lee-side glacier occurred (Fig. 1b). Currently, only the remains of past glaciation have been observed (Vieira and Ferreira, 1998). The LGM of the Serra da Estrela (LGMSE) is estimated to have occurred at ca. 33.1 ± 5.0 to 30 ± 4.5 ka BP (Vieira, 2008); and geomorphological evidence of glacial activity in the Serra da Estrela in MIS 6 at 140 ka BP has been found at the Lagoa Seca col. (Vieira et al., 2021).

The main records of landscape history after deglaciation are from sediment cores from the Charco da Candieira cores at 1400 m a.s.l. (Van den Brink and Janssen, 1985; Van der Knaap and Van Leeuwen, 1995, 1997; Connor et al., 2012) and from the Lake Peixão at 1677 m a.s.l. The sediment cores of Candieira revealed six phases of environmental

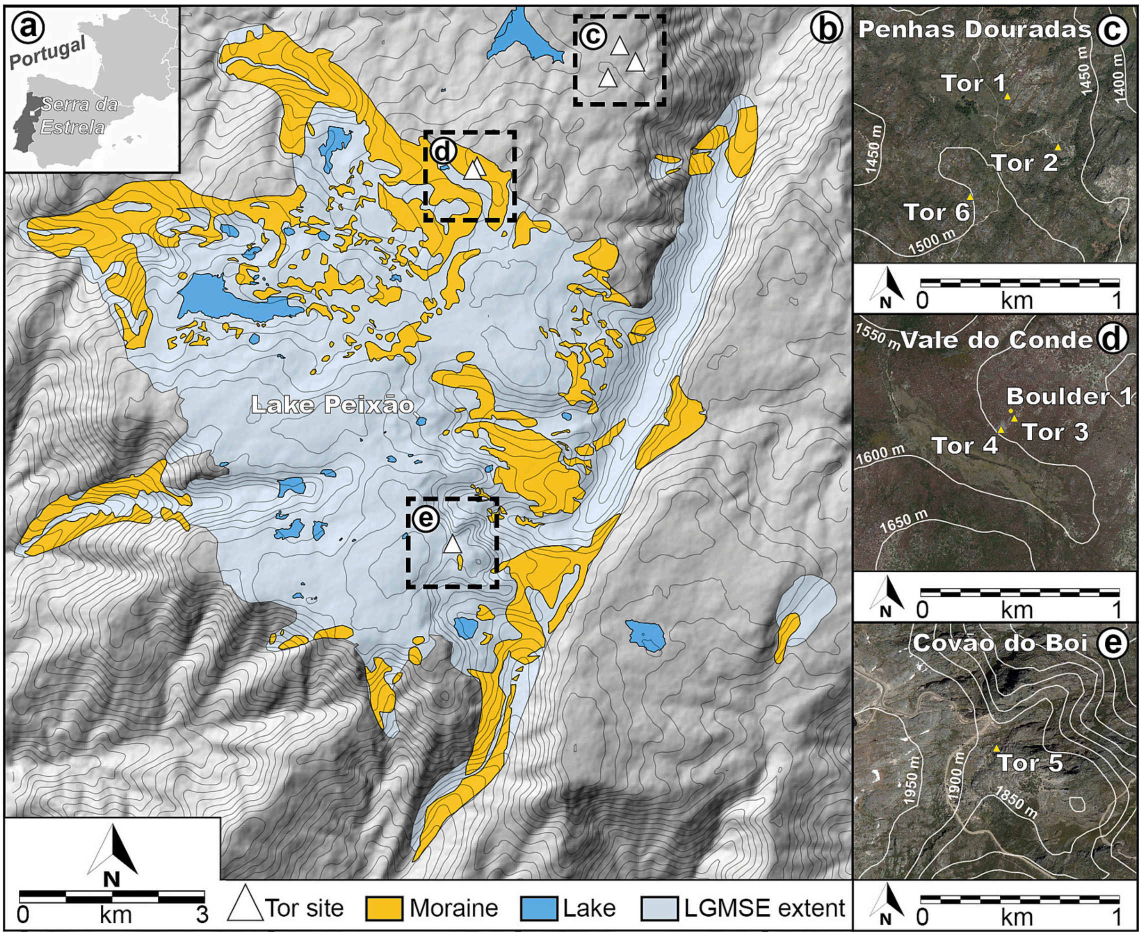

Fig. 1. (a) Position of the Serra da Estrela upland in Portugal, Europe. (b) Map of the Serra da Estrela after Vieira (2004) illustrating the last glacial maximum of the Serra da Estrela (LGMSE, ca. 33.1 ± 5.0 to 30 ± 4.5 ka BP; Vieira, 2008) and today moraine deposits. Satellite images (Google Earth, 2021) of the sampling sites and indication of selected tors in the (c) non-glaciated area at Penhas Douradas, and formally glaciated areas at the (d) Vale do Conde and (e) Covão do Boi, including the position of the moraine boulder (d) from previous investigations (Raab et al., 2022).

changes (Van der Knaap and Van Leeuwen, 1995, 1997) from 14.8 ka to 40 a cal BP. Sediment core analyses by Connor et al. (2012) showed that forest and bush fires have been frequent in the Serra da Estrela since the Late Glacial and are, thus, part of the regional ecological dynamics. Charcoal records exhibited two major periods of increased fire activities one at the onset of the Holocene (~12–11 ka cal BP) and one during the mid-late Holocene (~3.5–2.5 ka cal BP). Geochemical and mineralogical data from sediment cores of the Lake Peixão (Fig. 1b) indicated that the periods between 14.40 and 13.76 ka cal BP and between 10.80 and 10.26 ka cal BP were characterized by low-frequency rainstorm-triggered flood events which is coherent with lower air temperatures, thicker and longer-lasting snow covers (Moreno et al., 2023). The lake sediments further revealed that an enhanced atmospheric dust deposition occured during cold periods. Speleothem records from Torres Novas (Portugal) have shown increased winter rainfall between 10 and 4 ka BP (Benson et al., 2021).

Recent soil investigations by Raab et al. (2022) highlighted a clear difference in soil formation between formerly glaciated areas (FGA) and non-glaciated areas (NGA). Short-term (last ~60 years) redistribution rates suggest high erosion rates of ~900 [t km^{-2} yr^{-1}] in NGA and deposition rates of ~230 [t km^{-2} yr^{-1}] in FGA. Multi-millennial erosion rates were calculated and were between 101 and 140 [t km^{-2} yr^{-1}] for NGA and 176–248 [t km^{-2} yr^{-1}] for FGA. The onset of soil formation for FGA was estimated to be around 22 ka (at ~1649 m a.s.l.). The soil age in NGA was estimated to range between 30 to over 100 ka.

2.2. Sampling sites

We investigated six tors in detail (Fig. 1.b; Fig. 2a-e; Fig. 3a-e), with three positioned in FGA and three located in NGA. Tors 1, 2 and 6 are in the northern part of Penhas Douradas plateau, which has never been glaciated and represents an undulating granite surface, with a range of medium-size residual landforms: large domes, tors, rock platforms, scattered and clustered boulders. The granite is muscovite-biotite coarse-grained porphyritic and locally named the Seia granite. In between bedrock elevations broad valleys and semi-enclosed shallow basins occur. A mantle of weathered granite (grus) of variable thickness (1–>5 m) discontinuously covers the bedrock, pointing to the important role of deep weathering in landscape evolution. Thus, the plateau may be interpreted as an exposed weathering front – an etch surface (Thomas, 1989), although deep weathering and stripping are ongoing processes.

Tor 1 is situated at c. 1500 m a.s.l. in the northern part of the plateau, crowning a low elevation, one of many within the plateau and typified by low bedrock outcrops, mainly shields and boulder piles. It represents a transition between a castle koppie (castellated tor) and a low dome. The outline and shape of the tor reflect two intersecting nearly vertical joint sets, running SW–NE and WNW–ESE, although vertical rock faces occur side by side with steeply dipping, convex surfaces. The third joint set is nearly horizontal, slightly dipping to the south, supporting steps and flattened top of the tor, with spacing of a few metres. Weathering and gravity tensile stresses have resulted in the opening of several

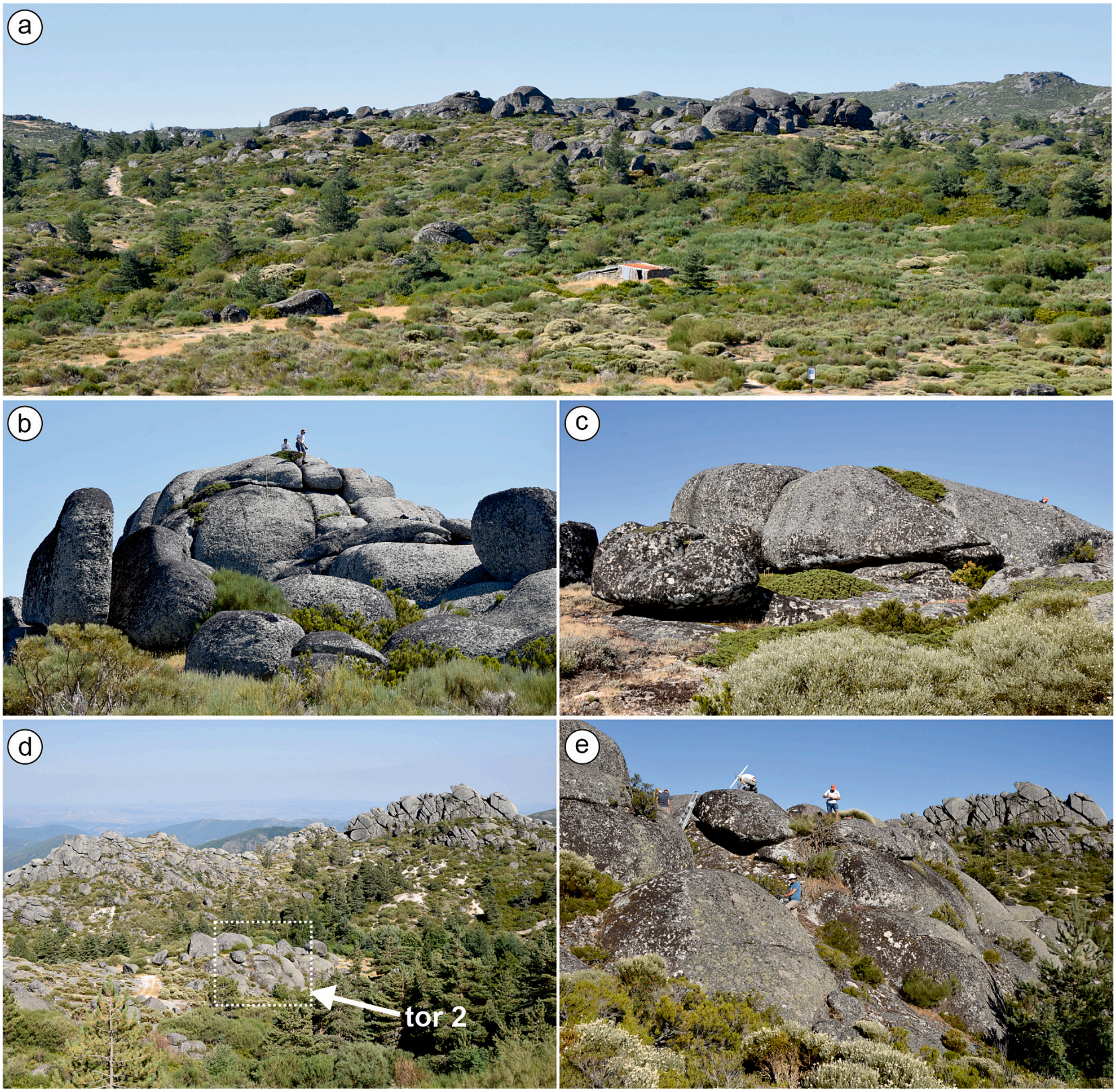

Fig. 2. Landscape impressions of the field sites (a) Penhas Douradas (b) Tor 1, (c) Tor 6, (d) top view, and (e) side-view of Tor 2.

vertical joints and outward tilting of rock slabs. One can therefore hypothesize that the main pathway of tor degradation is block-by-block, although granular disintegration undoubtedly occurs too, as testified by the aprons of grus around the tor and, indirectly, by rounded outlines of individual rock blocks. The tor is ca. 60 m long in SW–NE direction and up to 20 m wide. Except the top sample, all other samples were collected within the SW-facing, steep and convex rock surface, within an elevation range of 10 m.

Tor 2 is located at c. 1448 m a.s.l. in the plateau marginal zone, just above the steep slope connecting with the bottom of the intramontane Manteigas Basin, where a minor, funnel-shaped basin is inset. The sloping floor of the basin is surrounded by rock and boulder-covered slopes alternating with shallow valleys excavated in grus. The depth of the basin is ca. 20 m. The tor occupies a hillslope position and is distinctively asymmetric, 3 m high on the upslope side, but 12 m high on the opposite side. The morphology indicates an emerging dome, with several convex sections one above another and the uppermost one reduced to a group of residual boulders. Although SW–NE-trending vertical joints cut the outcrop, no evidence of block-by-block breakdown is present around the outcrop and the principal pathway of tor decay is probably granular disintegration with grus removal promoted by fluvial incision. The locality is inferred to be subject to faster degradation than Tor 1 because of higher available relief and an available route of efficient removal of weathering products down the slope to the basin floor and beyond, towards the Zêzere Valley. Samples were collected along a transect on the SW-facing slope, within an elevation range of 9 m.

Tor 6 occurs more to the south with respect to Tors 1 and 2, within an undulating plateau surface dotted with numerous low (<10 m) bedrock elevations. These elevations are of two kinds: convex shield-like and groups of isolated boulders, in places resting on a convex slab or shield. Tor 6 represents a shield-like outcrop (low dome), ca. 20 m × 20 m, undercut on the NW side by a low cliff developed along a SW–NE-trending joint. Hence, the outcrop is asymmetric, 3.5 m on the SE side and 6 m on the NW side. Two vertical joints intersect the top part of the

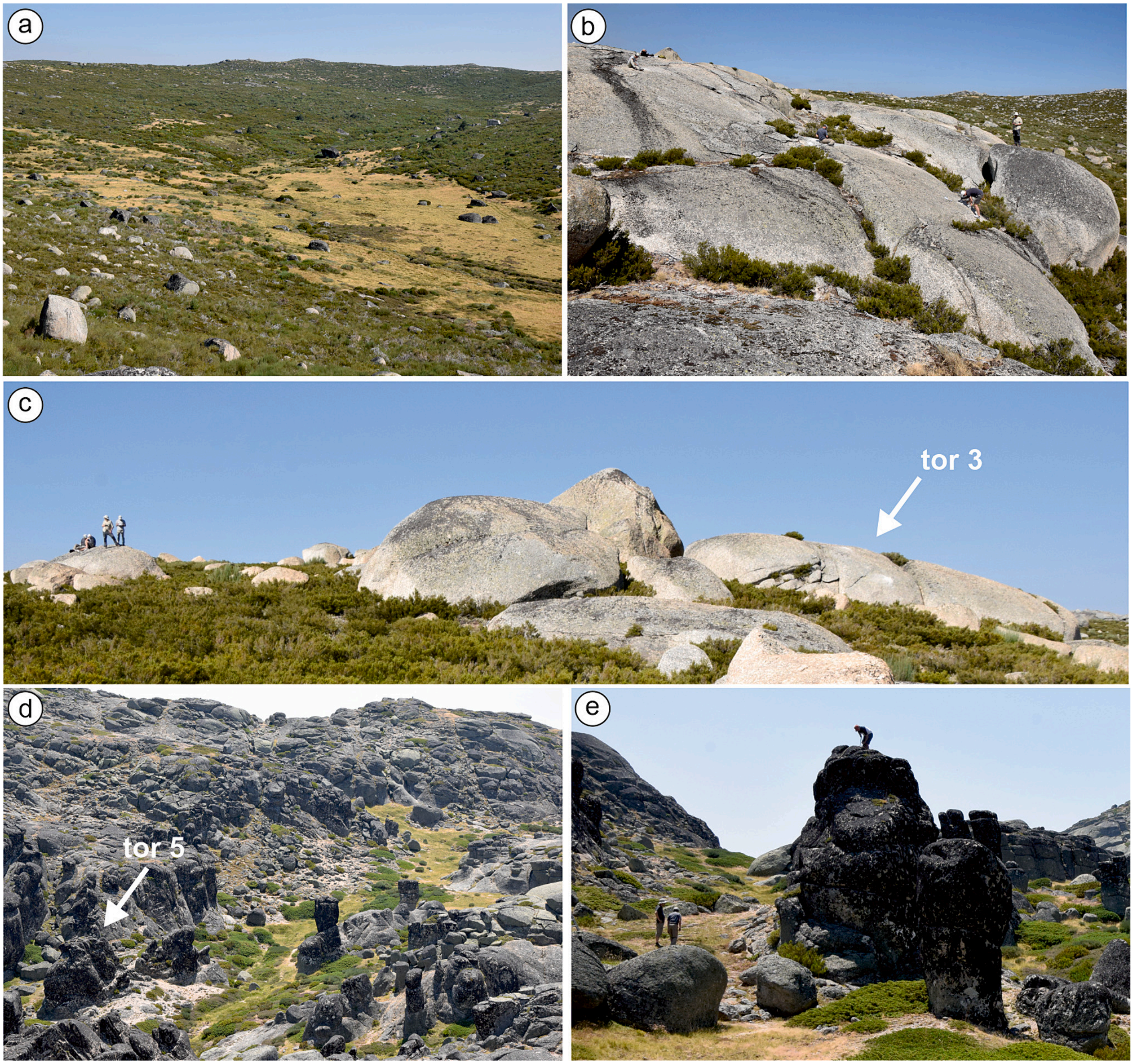

Fig. 3. Landscape impressions of the field sites (a) Vale do Conde (b) Tor 4 (c) Tor 3, and people taking samples of Boulder 1 (d), view of the Covā do Boi (e) side-view of Tor 5.

dome, but there is no evidence of block release and displacement. Rather, sustained granular disintegration is the main process of tor decay. Samples were collected along a transect on the N-facing slope, within the elevation range of 6 m. The geomorphic setting of the tor suggests that the rates of erosion would be low, perhaps comparable to Tor 1, but significantly lower than at Tor 2.

Tors 3 (1638 m a.s.l) and 4 (1630 m a.s.l) are located further to the south, on the northern shoulder of Vale do Conde, which is a shallow valley inset into the plateau surface, also within the Seia granite. Moraine boulders inside the valley indicate that one of outlet glacial tongues radiating from the plateau ice-field used the valley, filling it almost up to the altitude of the local divide on the northern side. Thus, both outcrops 3 and 4 have been under glacier ice for some time. One moraine boulder located nearby was dated by Raab et al. (2022) and yielded cosmogenic exposure age of 22 ± 2 ka.

Tor 3 is a low asymmetric outcrop, <2 m high on the upslope side but 4 m high on the downslope side. It is 20 m × 12 m, extended NW–SE. Morphologically it represents a smooth, partly emergent dome, cut through by a few SW–NE-trending joints, but lacking subhorizontal joints. On the top surface two weathering pits (see also Dominguez-Villar et al., 2009) occur, 105 cm × 90 cm and 70 cm × 60 cm, respectively. Their depth is 10–15 cm. Samples were collected along a transect on the SW-facing slope, within an elevation range of 4 m. The rock surface shows no signs of glacial scouring, which may be due to the coarse-grained granite not prone to conservation of glacial abrasion features, a typical situation in the Serra da Estrela.

A much larger outcrop 4 is situated ca. 60 m to the south-west down the slope, at lower elevation and within a steeper slope section than Tor 3. The outcrop is ca. 55 m × 50 m, with the height of 12 m. Morphologically it may be classified as bedrock knob or a half-dome, partly emergent from the slope, with several convex section one above another, separated by narrow, partly vegetated ledges. Smooth surfaces are cut by several SW–NE-trending joints, whereas some WNW–ESE-trending joints open in response to tensile stresses forming narrow clefts up 2 m deep. Evidence of exfoliation is present in the form of surface-parallel cracks at shallow depth and detached thin sheets of granite. However, no signs of displacement of large blocks were found. Samples were collected along a transect on the S-facing slope, within an elevation range of 10 m. As in Tor 3, the rock surface shows no signs of glacial scouring.

The setting of Tor 5 at Covão do Boi at c. 1860 m a.s.l., although also within a formerly glaciated terrain, is different from that of tors 3 and 4, with the bedrock being a muscovite-biotite medium-grained granite, locally named the Covilhã granite, and positioned within a fault zone. Tor 5 itself, a massive semi-angular outcrop 6 m high, rises from the floor of a linear basin, hanging high above the headwater reaches of glacial troughs of Zêzere and Alforfa. In ground plan it measures 13 m × 5 m, with the long axis controlled by SW–NE-trending joints. In the immediate vicinity many other castellated and columnar outcrops occur, whereas a similar height of their upper surfaces and rock platforms above the basin suggests the former position of the basin floor. Remnant pockets of grus in between tors and along jointed zones intersecting basin rims indicate the past existence of a mantle of deeply (potentially hydrothermally) weathered granite, with highly variable and non-uniform thickness. Similar elevation of several tor summit surfaces at the site and the presence of moraines in the vicinity led to the interpretation that they were razed by glaciers, followed by streamflow responsible for removal of the pre-glacial weathering products and exposure of columnar tors, which make the locality one of the most significant geosites of the Estrela UNESCO Global Geopark. These were in turn subject to further subaerial weathering (potentially favored by a local fault zone) that smoothed any joint-related edges, leading to the contemporary shape. Samples were collected along a transect on the SE-facing slope, within an elevation range of 6 m.

3. Materials and methods

3.1. Sampling design

The detailed sampling concept is outlined in Raab et al. (2018, 2019) and Raab (2019). In brief, vertical profiles were sampled of tors to derive surface exposure ages that allow the computation of surface denudation rates. Therefore, we took five to eight <2 kg samples of rock within the uppermost 1–3 cm of the rock surface at multiple heights per tor using an electric stone saw, chisel, and hammer. Each tor had a minimum height of four meters above ground (Table 1). When possible, we also took one sample below the soil surface to assess the early subsurface accumulation of the TCN. Each sampling site was recorded by DGPS (differential global position system) and verified with topographic maps. The individual geometry of each tor was recorded with detailed 3D drone models with accuracy better than 10 cm and field data of topographic shielding, dip, and dip-direction of the sampled rock surfaces were collected (Table 1).

3.2. Laboratory procedures for surface exposure dating (^{10}Be)

All 37 rock samples were individually crushed and about 0.4 kg of the 0.25–0.6 mm fraction was retained. The material was then processed according to standard practice (Kohl and Nishiizumi, 1992), summarised as follows. The fraction was treated using *aqua regia* (1:4.22 of 65 % HNO_3 to 32 % HCl) for up to 36 h to eliminate iron oxides, organic material and carbonates. The remaining mineral assemblage underwent a 1 h treatment with 0.4 % HF. A flotation system after Kitchener (1984) was used to physically separate mica and feldspar from quartz. The remaining contaminants were removed with 4 % HF leaching cycles (7–21 days). The resulting 30 g of pure quartz was spiked with a ^{9}Be-carrier solution (Scharlau, BE03460100) and dissolved in 40 % HF. We isolated Be using anion (Bio-Rad AG1-X8 resin) and cation (Bio-Rad AG50-X8 resin) exchange columns (von Blanckenburg et al., 1996).

The resulting $Be(OH)_2$ gel was dehydrated on a hot plate at 70 °C overnight and at 120 °C for ~5 h. The $Be(OH)_2$ was converted to BeO by calcination at 850 °C for two hours. The final BeO was mixed with niobium (Nb) powder prior to pressing into copper (Cu)-targets. The $^{10}Be/^9Be$ ratio was measured using a MILEA accelerator mass spectrometry (AMS) system at ETH Zurich (Maxeiner et al., 2019). The ETH used ^{10}Be standard S2007N and S2010N with a nominal value of $^{10}Be/^9Be = 28.1 \times 10^{-12}$ and $^{10}Be/^9Be = 3.3 \times 10^{-12}$ calibrated to the Nishiizumi standard ICN01–5-1 with a revised nominal value of 2.709×10^{-11} (Nishiizumi et al., 2007; Kubik and Christl, 2010; Christl et al., 2013). The 1σ error of S2007N and S2010N are 2.7 % (Christl et al., 2013) and 2.2 % respectively. Both standards have an associated ^{10}Be half-life of 1.387 ± 0.012 Myr (Chmeleff et al., 2010; Korschinek et al., 2010) The measured $^{10}Be/^9Be$ ratios were corrected for the ^{10}Be contribution of the Be-carrier (*^{10}Be*: Scharlau BE03460100 2096, BATCH: 17373701, $^{10}Be/^9Be$ blank ratio: $7.45 \pm 13.55 \times 10^{-16}$).

3.3. Determination of exposure ages and surface denudation using ^{10}Be

The exposure ages were calculated using rock erosion rates of 0–2 [mm kyr^{-1}] (Table 2). We used the shielding calculator of Tikhomirov et al. (2014) to account for the tor geometry (Table S2 provides alternative surface ages based on the online shielding calculator). We used the cosmogenic nuclide online calculator v3.0 (Balco et al., 2008; Balco, 2017) to calculate the ages. The program uses a ^{10}Be half-life of 1.387 ± 0.0012 Ma (Chmeleff et al., 2010; Korschinek et al., 2010) and a sea-level high latitude ^{10}Be production rate of 4.01 [^{10}Be-atoms gram SiO_2^{-1} year^{-1}] (Borchers et al., 2016). The production rate was corrected for latitude and altitude after the scaling scheme of Lifton et al. (2014). Furthermore, sample thickness correction was done following Brown et al. (1992), with an effective radiation attenuation length of 160 [g cm^{-2}] of Gosse and Philips (2001) and a constant rock density of 2.65 [g cm^{-3}]. No additional correction for snow was applied. Related effects of geomagnetic field variations on the in-situ ^{10}Be ages can be assumed to be negligible (Masarik et al., 2001; Pigati and Lifton, 2004).

The tor exposure/exhumation models were based on the best regression fits. We used the logistic function after Lichter (1998) and polynomial functions to quantify the $D_{Surface}$ ranges. The height-age relation of the exposed tors was modelled by taking the error ranges of the surface exposure ages and sample height measurements into account, using Monte Carlo simulations. The mathematical derivative of these functions determined the exhumation rate and, thus, surface denudation rates over time ($D_{Surface}$). When applicable, we accounted for the rock subsurface accumulation of TCNs following Raab et al. (2018). Exceptionally young or old ages compared to the neighbouring samples along the age profiles were excluded from the models (e.g., Tor 2, Tor 6).

3.4. Ultra-high resolution tor photogrammetric models

A photogrammetric drone-based survey of the sampled tors was conducted to accurately characterize the terrain, locate the sampling spots and support the interpretation of results. We used a Mavic 2 Pro flying at 40–60 m height and conducted surveys using nadir photography and parallel flight lines in the simple tors and crossed-flight lines and oblique photography in the more complex tors morphologies. Ground control points were collected using a differential GNSS survey in RTK mode using a GSM connection and the national network of permanent stations (RENEP) for positioning. This was done at all tors, except Tor 5, where we used non-corrected coordinates for the model. In locations without mobile phone network, we used a base station, surveyed in RTK mode and post-processed the coordinates using NRCAN Precise Point Positioning. The procedure resulted in accuracies of 3 to 5 cm using independent check points. 3D point clouds, 3D meshes, orthomosaics and digital surface models were obtained using PIX4-mapper. Ground sampling distances varied from 0.9 to 1.5 cm and maximum root mean square errors were of 5.6 cm in easting and northing to 6.8 cm in elevation. These ultra-high-resolution models are made available as supplementary materials.

Table 1
Sample characteristics of the investigated six tor profiles. Tor and sample positions have been established using a differential global positioning system (DGPS) and 3D drone modelling (See Fig. 2). Sample thicknesses have been calculated on the weighted average of the rock chips, which has been confirmed by the cut surface depth measured in the field. We provide the traditional shielding parameter after Balco (2018) and secondary shielding values after Tikhomirov et al. (2014) that incorporate self-shielding due to the tor geometry.

Samples series	DGPS Coordinates [WGS84]		Elevation of samples from DGPS			Sample thickness	Surface angle	Aspect	Shielding factor (Balco 2018)	Shielding factor (Tikhomirov et al., 2014)	Cut surface		Heights above ground			
	Latitude	Longitude			Error						Field measured span	Actual vertical difference (surface angle corrected)	average		Range based on cut surface field measures	Incl. DGPS error range
	[°N]	[°W]	[m a.s.l.][+]		[m]	[cm]	[deg]	[deg]	[−]		[cm]	[cm]	[cm]		[cm]	[cm]
Tor 1																
Tor-1-1-Top	40.3974	−7.5665	1501.52	±	0.02	1.00	10	290	0.99934	0.98962	23	4.0	1099.54	±	2.00	4.23
Tor-1-2-Upper Middle	40.3974	−7.5665	1499.82	±	0.02	1.50	30	260	0.97741	0.95680	15	7.5	929.54	±	3.75	5.99
Tor-1-3-Middle	40.3973	−7.5666	1496.88	±	0.02	1.25	50	250	0.89163	0.86595	20	15.3	634.74	±	7.66	9.90
Tor-1-7	40.3973	−7.5666	1494.84	±	0.02	1.20	60	270	0.81752	0.79062	17	14.7	431.44	±	7.36	9.60
Tor-1-4-Lower Middle	40.3973	−7.5666	1492.63	±	0.02	1.00	71	255	0.70875	0.68280	20	18.9	209.84	±	9.46	11.69
Tor-1-5-Bottom	40.3973	−7.5666	1491.30	±	0.02	1.00	71	255	0.70875	0.68280	20	18.9	77.44	±	9.46	11.69
Tor-1-6-Subsurface	40.3973	−7.5666	1490.43	±	0.02	1.40	71	255	0.70875	0.67519	20	18.9	−9.46	±	9.46	11.69
Tor-2-1-Top	40.3950	−7.5635	1448.40	±	0.07	1.50	0	0	0.99674	0.98300	0	1.5	907.40	±	0.75	7.43
Tor-2-2-Upper Middle	40.3950	−7.5635	1447.19	±	0.07	1.00	37	255	0.95456	0.93822	16	9.6	786.30	±	4.81	11.49
Tor-2-3-Middle	40.3950	−7.5635	1445.10	±	0.07	1.20	55	245	0.85479	0.82930	21	17.2	577.60	±	8.60	15.28
Tor-2-7 - Between 3 and 4	40.3950	−7.5636	1441.60	±	0.07	3.50	40	267	0.94155	0.89023	21	13.5	227.70	±	6.75	13.42
Tor-2-4-Lower Middle	40.3950	−7.5636	1441.05	±	0.07	1.00	58	230	0.71800	0.69888	18	15.3	173.00	±	7.63	14.31
Tor-2-8 - Between 4 and 5	40.3950	−7.5636	1440.42	±	0.07	1.50	65	235	0.71623	0.68658	25	22.7	110.00	±	11.33	18.00
Tor-2-5-Bottom	40.3950	−7.5636	1439.55	±	0.07	1.20	73	245	0.63463	0.61286	26	24.9	23.00	±	12.43	19.11
Tor-2-6-Subsurface	40.3950	−7.5636	1439.40	±	0.07	1.60	90	240	0.49576	0.46140	16	16.0	8.00	±	8.00	14.68
Tor-3-1-Top	40.3801	−7.5942	1638.29	±	0.07	1.50	10	215	0.99919	0.98471	12	2.1	421.72	±	1.04	8.11
Tor-3-2-Upper Middle	40.3801	−7.5942	1637.71	±	0.07	1.00	15	205	0.99740	0.98697	20	5.2	364.42	±	2.59	9.66
Tor-3-3-Middle	40.3800	−7.5942	1636.18	±	0.07	1.70	55	210	0.85717	0.82290	22	18.0	211.42	±	9.01	16.08
Tor-3-5-Bottom	40.3800	−7.5942	1634.53	±	0.07	1.40	77	215	0.64827	0.61467	17	16.6	46.42	±	8.28	15.35
Tor-3-6-Subsurface	40.3800	−7.5942	1634.00	±	0.07	1.00	90	220	0.49963	0.47582	14	13.2	−6.58	±	6.58	13.65

(*continued on next page*)

Table 1 (*continued*)

Samples series	DGPS Coordinates [WGS84]		Elevation of samples from DGPS			Sample thickness	Surface angle	Aspect	Shielding factor (Balco 2018)	Shielding factor (Tikhomirov et al., 2014)	Cut surface		Heights above ground			
	Latitude	Longitude			Error						Field measured span	Actual vertical difference (surface angle corrected)	average		Range based on cut surface field measures	Incl. DGPS error range
Tor-4-1-Top	40.3798	−7.5949	1631.98	±	0.07	2.00	12	250	0.99883	0.97919	16	3.3	1190.16	±	1.66	8.73
Tor-4-2-Upper Middle	40.3797	−7.5949	1630.22	±	0.07	1.80	15	210	0.99753	0.97902	22	5.7	1014.36	±	2.85	9.92
Tor-4-3-Middle	40.3796	−7.5949	1626.58	±	0.07	1.50	20	190	0.99383	0.97688	25	8.6	650.36	±	4.28	11.35
Tor-4-4-Lower Middle	40.3796	−7.5950	1624.42	±	0.07	1.00	25	190	0.98727	0.97448	19	8.0	434.36	±	4.01	11.09
Tor-4-5-Bottom	40.3796	−7.5950	1622.05	±	0.07	1.60	50	175	0.88718	0.85651	18	13.8	197.36	±	6.89	13.97
Tor-4-6-Subsurface	40.3795	−7.5950	1620.12	±	0.07	1.25	20	175	0.97162	0.95842	22	7.5	3.76	±	3.76	10.83
Tor-5-1-Top	40.3251	−7.5999	1865.38	±	n.d	2.70	15	120	0.99264	0.96540	19	4.9	564.30	±	2.46	n.d*
Tor-5-2-Upper Middle	40.3251	−7.5999	1863.46	±	n.d	2.50	88	160	0.51135	0.46377	20	20.0	372.30	±	9.99	n.d*
Tor-5-3-Middle	40.3251	−7.6000	1862.31	±	n.d	2.00	75	175	0.61460	0.58124	20	19.3	257.30	±	9.66	n.d*
Tor-5-4-Lower Middle	40.3251	−7.6000	1861.22	±	n.d	1.66	68	170	0.69012	0.66381	15	13.9	148.30	±	6.95	n.d*
Tor-5-5-Bottom	40.3251	−7.5999	1859.84	±	n.d	1.75	90	150	0.48096	0.43895	20	20.0	10.00	±	10.00	n.d*
Tor-6-1-Top	40.3927	−7.5688	1530.46	±	0.43	1.30	0	0	0.99996	0.98819	19	1.3	845.15	±	0.65	43.66
Tor-6-7-Top-2	40.3928	−7.5689	1529.98	±	0.43	1.50	5	10	0.99992	0.98612	30	2.6	797.15	±	1.31	44.32
Tor-6-2-Upper Middle	40.3928	−7.5689	1528.87	±	0.43	1.50	17	345	0.99637	0.98031	17	5.0	685.85	±	2.49	45.50
Tor-6-3-Middle	40.3928	−7.5689	1527.64	±	0.43	1.70	24	335	0.98893	0.96835	22	8.9	563.15	±	4.47	47.49
Tor-6-4-Lower Middle	40.3929	−7.5689	1526.07	±	0.43	1.25	45	260	0.91779	0.89377	21	14.8	406.15	±	7.42	50.44
Tor-6-5-Bottom	40.3929	−7.5689	1524.14	±	0.43	1.00	10	290	0.98583	0.97622	27	4.7	213.15	±	2.34	45.36
Tor-6-6-Subsurface	40.3929	−7.5689	n.d		n.d	1.20	80	270	0.29910	0.26894	20	19.7	−9.85	±	9.85	n.d

+ Meter above sea level.
* n.d. = no data.

Table 2
Summary of in-situ ^{10}Be content and derived surface exposure ages. Errors for measured isotope contents are given in1-σ, and surface exposure ages in 2-σ. Surface exposure ages were calculated with CRONUS age calculator v3 (Balco et al., 2008; Balco, 2017) using the shielding calculator after Tikhomirov et al. (2014), and the LSDm model (Lifton, Sata, Dunai, 2014). Ages for three different rock erosion rates are presented. Further ages model results are found int Table S1. Ages are calculated without correction for snow cover or glacial isostatic adjustment (GIA). We report separating age uncertainties. The measurement's analytical uncertainty (A.-Error) and the total uncertainty include the nuclide production rate uncertainty (P.-Error). The A.-Error compares how well the exposure ages within one tor profile agree. The P.-Error is used to compare the diverse locations.

					Calculated Surface Exposure Ages (LSDm) - Shielding after Tikhomirov et al., 2014											
Samples series	^{10}Be content 10^4 [atomg^{-1} yr^{-1}]			Error [%]	0 [mm kyr^{-1}] Average		A.-Error	P.-Error	1 [mm kyr^{-1}] Average		A.-Error	P.-Error	2 [mm kyr^{-1}] Average		A.-Error	P.-Error
Tor 1 (NGA)																
Tor-1-1-Top	167.89	±	4.92	2.93	129′231	±	3′908	8′793	146′205	±	5′032	11′320	171′150	±	7′068	15′900
Tor-1-2-Upper Middle	131.75	±	3.86	2.93	106′412	±	3′204	7′200	116′426	±	3′879	8′719	129′874	±	4′926	11′072
Tor-1-3-Middle	108.99	±	3.20	2.93	97′826	±	2′942	6′606	106′012	±	3′495	7′848	116′618	±	4′309	9′676
Tor-1-7	91.91	±	2.72	2.96	90′842	±	2′747	6′133	97′846	±	3′219	7′188	106′545	±	3′884	8′673
Tor-1-4-LowerMiddle	41.04	±	1.26	3.07	45′545	±	1′413	3′063	47′867	±	1′547	3′353	50′395	±	1′704	3′695
Tor-1-5-Bottom	23.00	±	0.86	3.72	25′834	±	967	1′813	26′374	±	1′009	1′893	26′987	±	1′057	1′982
Tor-1-6-Subsurface	16.06	±	0.60	3.77	18′798	±	711	1′322	19′081	±	734	1′363	19′376	±	757	1′408
Tor 2 (NGA)																
Tor-2-1-Top	61.70	±	1.84	2.98	50′736	±	1′530	3′396	53′577	±	1′691	3′753	56′364	±	1′872	4′155
Tor-2-2-UpperMiddle	94.94	±	2.80	2.95	82′243	±	2′478	5′539	88′314	±	2′872	6′418	95′406	±	3′397	7′591
Tor-2-3-Middle	70.27	±	2.07	2.94	68′699	±	2′058	4′609	73′155	±	2′334	5′225	78′120	±	2′680	6′001
Tor-2-7-Between3and4	40.05	±	1.26	3.14	36′840	±	1′166	2′484	37′996	±	1′242	2′646	39′180	±	1′325	2′823
Tor-2-4-LowerMiddle	27.30	±	1.03	3.78	31′041	±	1′181	2′191	31′968	±	1′250	2′318	33′017	±	1′329	2′465
Tor-2-8-Between4and5	21.78	±	0.83	3.80	25′456	±	974	1′798	25′991	±	1′016	1′876	26′545	±	1′062	1′961
Tor-2-5-Bottom	14.79	±	0.67	4.51	19′734	±	894	1′473	20′042	±	923	1′521	20′367	±	955	1′573
Tor-2-6-Subsurface	6.88	±	0.32	4.61	12′556	±	581	943	12′670	±	593	962	12′787	±	604	981
Tor 3 (FGA)																
Tor-3-1-Top	133.72	±	3.92	2.93	95′021	±	2′852	6′411	102′729	±	3′370	7′576	112′488	±	4′117	9′253
Tor-3-2-UpperMiddle	140.57	±	4.12	2.93	98′978	±	2′973	6′684	107′373	±	3′540	7′959	118′352	±	4′382	9′853
Tor-3-3-Middle	83.41	±	2.45	2.94	71′044	±	2′126	4′767	75′772	±	2′419	5′426	81′200	±	2′798	6′273
Tor-3-5-Bottom	24.64	±	0.83	3.36	27′481	±	929	1′879	28′116	±	974	1′968	28′790	±	1′022	2′066
Tor-3-6-Subsurface	18.09	±	0.65	3.58	25′925	±	933	1′800	26′466	±	974	1′879	27′087	±	1′021	1′969
Tor 4 (FGA)																
Tor-4-1-Top	25.96	±	0.86	3.31	18′935	±	629	1′287	19′221	±	649	1′327	19′522	±	670	1′371
Tor-4-2-UpperMiddle	24.70	±	0.82	3.31	18′065	±	601	1′228	18′334	±	619	1′265	18′609	±	639	1′305
Tor-4-3-Middle	23.13	±	0.79	3.44	17′022	±	587	1′167	17′253	±	604	1′200	17′495	±	622	1′235
Tor-4-4-LowerMiddle	27.41	±	0.95	3.48	19′960	±	698	1′374	20′279	±	722	1′420	20′609	±	746	1′469
Tor-4-5-Bottom	16.93	±	0.64	3.79	14′381	±	548	1′012	14′550	±	561	1′037	14′731	±	575	1′063
Tor-4-6-Subsurface	15.49	±	0.64	4.15	12′010	±	500	869	12′109	±	509	885	12′213	±	518	902
Tor 5 (FGA)																
Tor-5-1-Top	16.78	±	0.63	3.76	10′994	±	415	772	11′086	±	422	785	11′180	±	430	799
Tor-5-2-UpperMiddle	6.51	±	0.34	5.19	8′906	±	464	702	8′994	±	472	714	9′085	±	480	727
Tor-5-3-Middle	5.58	±	0.28	4.99	5′984	±	299	463	6′013	±	302	468	6′042	±	305	473
Tor-5-4-LowerMiddle	6.62	±	0.33	4.93	6′228	±	308	480	6′267	±	311	485	6′305	±	315	491
Tor-5-5-Bottom	4.21	±	0.26	6.18	5′949	±	368	509	5′976	±	372	514	6′005	±	376	519
Tor 6 (NGA)																
Tor-6-1-Top	246.64	±	7.23	2.93	188′314	±	5′786	13′008	225′505	±	8′509	19′130	298′267	±	16′276	36′592
Tor-6-7-Top-2	300.21	±	8.79	2.93	230′174	±	7′141	16′066	292′512	±	11′933	26′848	463′545	±	37′276	83′864
Tor-6-2-UpperMiddle	152.86	±	4.49	2.94	117′139	±	3′546	7′952	129′784	±	4′401	9′871	148′611	±	5′876	13′178
Tor-6-3-Middle	96.76	±	2.86	2.95	76′474	±	2′303	5′143	81′773	±	2′641	5′900	88′094	±	3′092	6′908
Tor-6-4-LowerMiddle	141.02	±	4.15	2.94	118′814	±	3′601	8′070	131′943	±	4′489	10′062	151′568	±	6′035	13′526
Tor-6-5-Bottom	54.67	±	1.63	2.98	41′672	±	1′255	2′784	43′148	±	1′348	2′989	44′830	±	1′458	3′232
Tor-6-6-Subsurface	13.23	±	0.54	4.05	36′148	±	1′478	2′611	37′245	±	1′572	2′776	38′416	±	1′677	2′961

3.5. Chemical weathering indices and optical microscopy

Chemical weathering indices characterize the weathering degree of rocks and soils using mineral alteration characteristics. While physical weathering breaks rocks and minerals apart, chemical weathering transforms primary minerals into secondary minerals (Parker, 1970). During the transformation, soluble elements are leached out over time. The fundamental principle of weathering indices is the natural depletion of mobile and relative enrichment of immobile elements.

We tested geochemical weathering proxies as potential relative exposure chronometers; among them was the often-used Chemical Index of Alteration (CIA; Nesbitt and Young, 1982), the Weathering Index of Parker (WIP; Parker, 1970), A-index (Kronberg and Nesbitt, 1981), and the B-index (Kronberg and Nesbitt, 1982). The results of all indices obtained from the same tor samples are listed in Table S4.

To calculate the weathering indices, the elemental composition of the rocks was determined by X-ray fluorescence (XRF) (Beckhoff et al., 2006). About 5 g of milled fine rock powder was analyzed as loose powder in sample cups using an energy-dispersive XRF spectrometer (SPECTRO X-LAB 2000, SPECTRO Analytical Instruments, Germany). An element standard (NCS DC 73326) was used for quality control. The loss on ignition (LOI) was determined by dry-ashing the milled fine rock powder (6 h, 1050 °C).

Thin sections (30 μm thick) were obtained from selected rock surface samples after impregnation with an epoxy resin and observed under a polarizing optical microscope in plane parallel (PPL) and cross polarized light (XPL). Major physical and chemical weathering features were described and mutually compared to estimate a relative degree of weathering.

4. Results

4.1. ^{10}Be content of tors

We investigated six tors with 37 successful measurements (Table 2, Table S2). The measured in-situ ^{10}Be contents ranged from 4.21 to 300.21 × 10^4 [atoms g^{-1}], averaging 65.72 × 10^4 [atoms g^{-1}]. The content error spans from 2.93 % to 6.18 % (Table 2). In general, the ^{10}Be content increases with tor height (Fig. 4a). Tor 5 and Tor 4 in FGA share a similar low content along their entire sampling profile in contrast to the other tors (Fig. 4a). Samples selected from tors in NGA resulted in higher ^{10}Be contents compared to samples from FGA. With elevation, the maximum ^{10}Be content of NGA tors increased but decreased among FGA tors (Fig. 4b). Contents below ~25 × 10^4 [atoms g^{-1}] were primarily found in FGA tor samples. Three samples taken below the soil surface (To1–6, To3–6, To6–6; Fig. 4c) had an average of 15.79 ± 0.6 × 10^4 [^{10}Be atoms g^{-1}].

4.2. Surface exposure ages

The surface exposure ages (± uncertainty) ranged from about 5.9 ± 0.5 to 230 ± 16 ka, considering a rock surface erosion rate of 0 [mm kyr^{-1}] (Table 2). Tors of FGA yielded ages a maximum of 99 ± 7 ka and a minimum of 5.9 ± 0.5 ka. Tors at NGA had a surface age ranging from 230.2 ± 16 to 12.6 ± 0.9 ka. The two tors with a consistently low ^{10}Be content throughout their vertical profiles (Fig. 4a; Tor 4 and Tor 5) gave ~12.6 ± 0.9 ka as a minimum age. The vertical age trends along the granite tor surface (Fig. 5a-f) finally reflect the ^{10}Be contents (Fig. 4a). All tors displayed a clear age-height pattern with only three inconsistent surface ages (To2–1, To4–4, To6–4). We assume that lower-than-expected age of To2–1 sample reflects ongoing disintegration of the top part of the tor, where massive rock surfaces are transformed into detached blocks. For To4–4 we assume that the inconsistency is related to glacial abrasion variations or the age stripping of overlying glacial debris, especially surface below around 18 ka (e.g.,To4–3, To4–5, To4–6) . The high age of To6–4 sample may be the result of sampling location near at the edge of the tor surface, where the TCN production rate may have been higher through multi-directional cosmic ray interaction. More minor age discrepancies, e.g., Tor 3 (samples To3–1 vs. To3–2), are within the error ranges of the adjacent samples.

4.3. Modelled (soil) surface denudation rates

The principal modelling assumption (Raab, 2019) of an increasing surface exposure age trend with tor height could be confirmed. Only three outliers (Tor-2-1, Fig. 6c; Tor-4-4, Fig. 7c and Tor-6-4, Fig. 6e) of 37 samples from the six tors were identified and excluded in the model calculations. Early subsurface cosmogenic nuclide accumulation correction has been applied for tors with samples below the ground level (see Fig. 4c), according to Raab et al. (2018). Given the age ranges

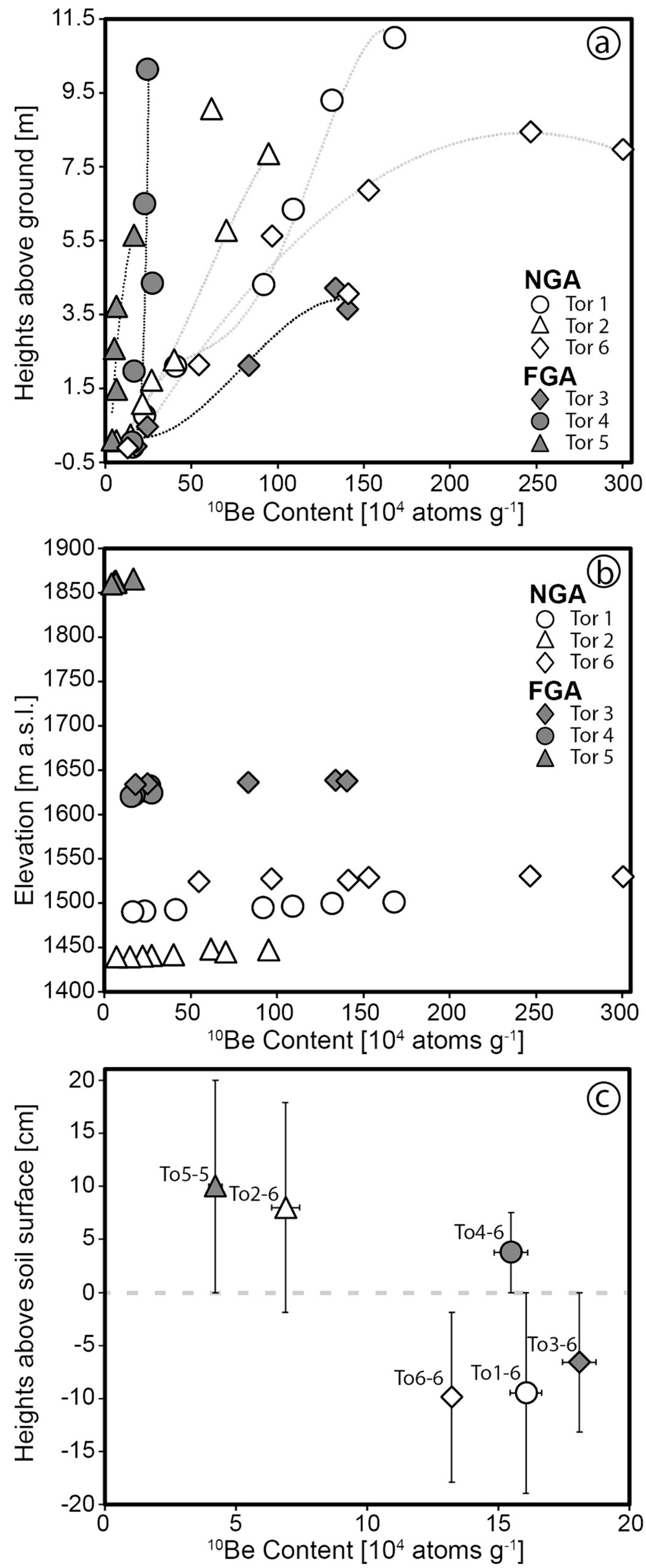

Fig. 4. Plots of ^{10}Be versus various parameters. (a) Measured ^{10}Be concentrations as a function of height above ground (with related trend curves) of all samples. (b) The ^{10}Be concentrations to elevation in meters above sea level (m a.s.l). (c) Detailed ^{10}Be concentration of samples close to or below the surface.

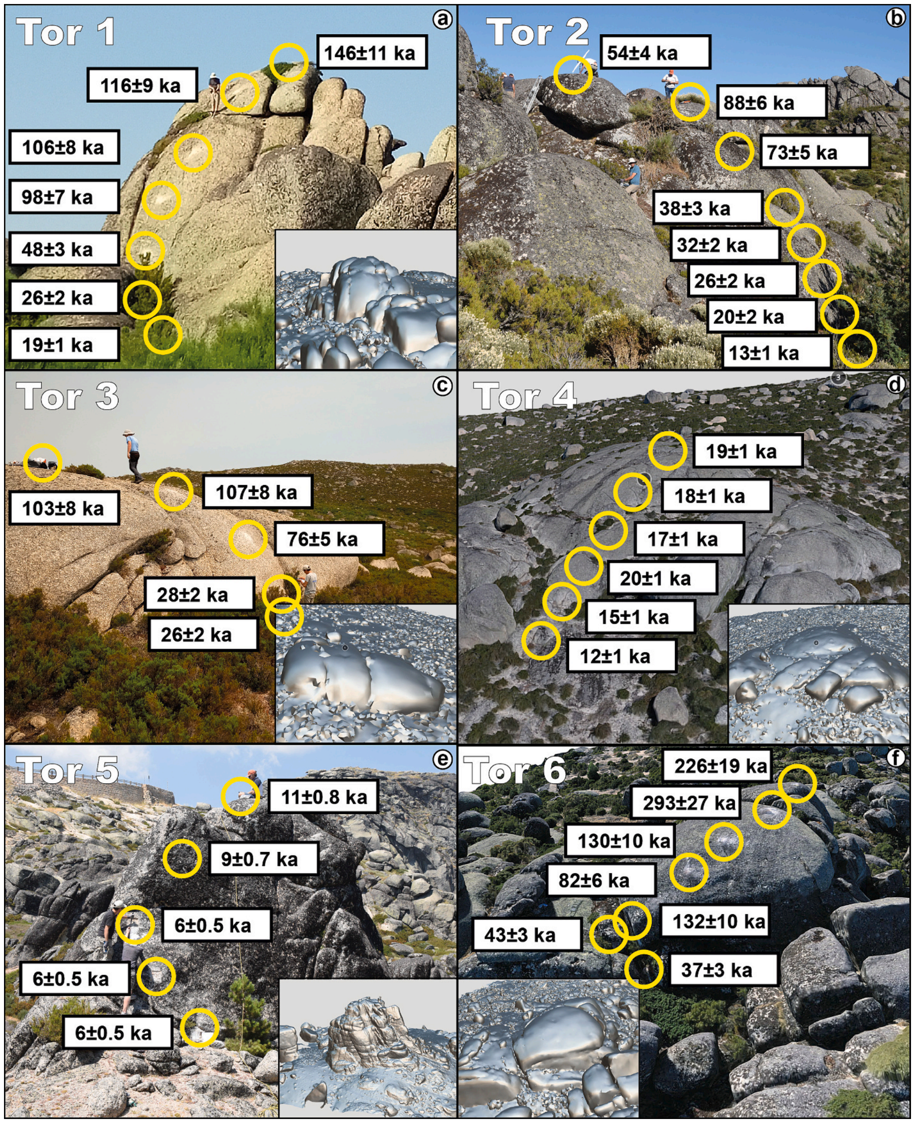

Fig. 5. Images and sample position of the investigated tors and their surface exposure ages (rock erosion of 1 [mm kyr^{-1}]) along their profiles (Table 2). Detailed 3D models are available (https://sketchfab.com/gtvieira) for a) Tor 1 at Penhas Dourads, b) Tor 2 also at Penhas Douradas for c) Tor 3 and d) Tor 4 at Vale do Conde, e) Tor 5 at Covão do Boi and f) Tor 6 at Alata Ribeira de Fervença. Detailed position data is found in Table S1.

provided in section 4.2, the model of NGA covers a more extended period and, thus more $D_{Surface}$ iterations. The $D_{Surface}$ ranges from about 0 to 0.53 [mm yr^{-1}] among NGA tors (Fig. 6a-f), and from 0 to 18.29 [mm yr^{-1}] among FGA tors (Fig. 7a-f).

Tor 1 and Tor 3 have alike individual trend patterns, both $D_{Surface}$ decreasing between ~40–80 ka, plateauing around 25–40 ka, and increasing again from ~25 ka until present, with all in the range of −0.02 to 0.25 [mm yr^{-1}]. The model of Tor 6 reflects a continuous increase of $D_{Surface}$ (Fig. 6f) since about 160 ka that coincides with the oldest modelled $D_{Surface}$ of Tor 1 (Fig. 6b). Tor 2 has the highest $D_{Surface}$ among NGA tors of up to 0.53 [mm yr^{-1}] and shares the decrease of $D_{Surface}$ since ~80 ka. Yet, Tor 2, reaches a near steady-state around 65 ka, followed by a relatively continuous $D_{Surface}$ of ~0.11 [mm yr^{-1}] until 12.5 ± 1 ka. Tors 4 and 5 present the highest $D_{Surface}$ within a quite restricted timeframe of around 14–20 ka and ~ 6 ± 0.3 ka, respectively.

4.4. Chemical rock weathering

Several chemical weathering indices (Table S4) calculated from the 37 XRF rock analyses (Table S3) present a lower weathering degree for NGA tors than FGA tors. (Fig. 8a,b). Only one index (Fig. 8c) showed the expected higher weathering degree to be found at NGA tors. The CIA and B-Index had the best age-correlations (p-test both 0.57). The weathering degree is highest at Tor 5 (FGA, sample To5–2) and lowest at Tor 1 (NGA, sample To1–3). Overall, in five out of six tors the weathering degree decreases with increasing heights, with the highest values in the subsurface samples. Tor 5 marks the exception where the degree of weathering, at least in part, increases with height above ground (Fig. 8a, b, c). The overall higher weathering degree of FGA tors is also reflected in the increase with elevation ($p = 0.77$; Fig. 8d). Thus, the highest weathering degree is found at ~1862 m a.s.l. The best correlation of weathering increase with elevation was found with the ratio of (Na + K)/Ti ($p = 0.84$; Fig. 8f). The relation of rock weathering to surface age remains challenging since the weathering degree mainly decreases with tor height, yet surface ages increase with heights above ground (Fig. 5a-g). This negative correlation ($p = -0.57$) is visualized in Fig. 6g.

4.5. Microscopic weathering features

The dominant mineral assemblage includes quartz and K-feldspar (mostly microcline), often affected by parallel alignment of intragrain individuals due to deformation, along with (occasionally zoned and/or

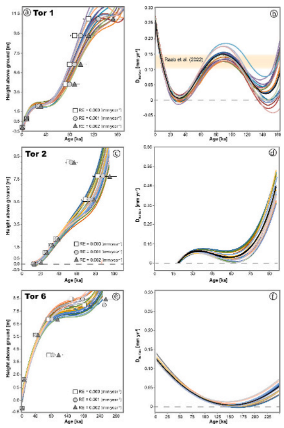

Fig. 6. Exposure ages as a function of tor height and derived surface denudation rates ($D_{Surface}$) based on Monte Carlo simulations for Tor #1 (a, b), Tor #2 (c, d) and Tor #6 (e, f) at non-glaciated area (NGA). Dark lines (b, d, f) reflect model averages. The yellow-coloured area in (b) indicates the percolation-theory-based multi-millennia erosion rates after Raab et al. (2022). RE = rock erosion.

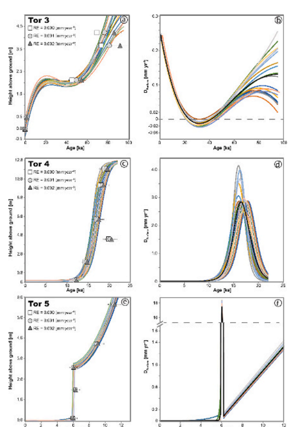

Fig. 7. Exposure ages as a function of tor height and derived surface denudation rates ($D_{Surface}$) based on Monte Carlo simulations for Tor #3 (a, b), Tor #4 (c, d) and Tor #5 (e, f) at formally glaciated area (FGA). Dark lines (b, d, f) reflect model averages. The dashed grey line (f) indicates the break in the y-axis for better display. RE = rock erosion.

sericitized) plagioclase, biotite and to a lesser extent muscovite (conversely prevailing in Tor 5), opaque minerals and very rare chlorite (Fig. 9). Sheared quartz displays wavy extinction between cross polarizers (and occasionally K-feldspar as well; Fig. 9a) and/or consists of polycrystalline grains (Fig. 9b, c). Major physical and chemical weathering patterns are recurrent, although with different extent, in all samples, independently from FGA and NGA sites. Strained crystals often display a preferential subparallel orientation of cracks aligned along the deformation directions or oblique in respect of these (Fig. 9a), which occasionally intersect with other crossed or randomly oriented fractures, in places widened and made coalescent by subsequent chemical dissolution. Quartz crystals often show sparse scratches and sometimes chemical dissolution pits (Fig. 9c). Feldspar and plagioclase exhibit dissolution features, which are scattered or concentrated along twinning planes and zonation (especially in the core), where also neoformed clays are found (Fig. 9d), and occasionally with a typical cavernous pattern (Fig. 9e). Micas are affected by common flaking and splitting along cleavage planes, in situ argillification and oxidation (Fig. 9f, g), starting from the edges and inter-flake voids to the entire crystals as long as weathering increases. Propagation of such microcracks into the surrounding minerals is usually observed, along with frequent migration of clay particles and Fe-oxides therein (Fig. 9f, g). In most weathered samples, illuvial clay and iron oxide coatings can be identified even far from (Fe-bearing) biotite grains, although they are poorly found in Tor 5. The mentioned features tend to increase with an increasing degree of weathering of each mineral species and consequently of the whole rock sample. In addition to mineral-specific weathering patterns, most of the samples display one or more sets of microcracks parallel to the rock surface (Fig. 9b), which appear thinner, shallower and mutually closer especially in the tors of FGA, where a shallower, denser, intersecting and occasionally crossed microcraking pattern is present as well (Fig. 9h). Tor 5 and Tor 6 exhibit the highest degree of weathering, whereas Tor 1 the lowest. Although with some uneven height-pattern, the overall degree of weathering tends to increase towards the intermediate and lower parts of the tors (Table 3).

5. Interpretation and discussion

To understand whether the TEA is suitable as an investigation tool for deriving multi-millennial surface denudation variability within formerly glaciated denudation zones, we discuss and interpret the results by focusing on the initial six hypotheses (I-VI) outlined in the introduction.

5.1. Tors selection quality and TEA applicability (Hypothesis I)

The surface exposure ages were within the range of former tor studies in non-glaciated and not significantly affected by cold-climate processes (e.g., 22.8–162.1 ka, Canberra, Australia, Heimsath et al., 2001a; 12 ± 1–106 ± 12 ka, Sila massif, Italy, Raab et al., 2019), periglacial (e.g., 9.2 ± 1–117.7 ± 6.6 ka, Dartmoor, England, Gunnell et al., 2013; 7.4 ± 0.3 to 107.5 ± 3.5 ka, Czech-Moravian Highland, Czechia, Máčka et al., 2023) and previously glaciated (e.g., 15.8 ± 3.1–297.0 ± 20.7 ka, Cairngorm Mountain, Scotland; Phillips et al., 2006) tor areas.

The increasing age trends with tor heights (Fig. 5a-f), with only three outliers (sections 4.2 and 4.3), unequivocally enabled us to use the tor exhumation/exposure approach (TEA) after Raab et al. (2018). The increased number of up to eight samples per tor (compared to past studies, usually four to six) highlighted the highly suitable conditions of the Serra da Estrela tors for the TEA. We could derive virtually continuous landscape-lowering rates in both NGA (Fig. 6b,d,f) and FGA (Fig. 7b,d,f). The quality of the dataset can be seen as an outcome of previous geomorphological mapping focused on tor distribution (Vieira, 2004; Migoń and Vieira, 2014) coupled with the reconstruction of past glacier extent in the Serra da Estrela by Vieira (2008), which both laid the foundation for the successful sampling campaign.

Within the moraine boulder field of the Vale do Conde, Tor 3 is located only 60 m northeast from Tor 4, and at a ~ 3–7 m higher elevation (Table 1). Yet, the Tor 3 maximum surface exposure age (~100 ka) is five times higher than the maximum age of Tor 4 (20 ± 1 ka). We consider that the age differences between Tor 3 and Tor 4 result from non-uniform glacial abrasion and striping of glacial debris, due to their positioning, Tor 4 being closer and lower in the glacial valley compared to Tor 3. The boulder field surrounding Tor 3 shows that the whole area was glaciated at 22.5 ± 2 ka ago (Raab et al., 2022). The difference in surface exposure ages shows that Tor 4 reveals the position of erosive ice extent that has shaped this glacial valley. In contrast, Tor 3 would have been located above this altitudinal limit, yet under thinner ice and located very close to the ice-field margin, which explains the low erosion (Fig. 11). Thus, in (formerly) glaciated landscapes, a detailed understanding of the glacial extent is a prerequisite before investigating surface denudation variations with the TEA. Yet tors are also a useful complementary proxy on ice extents and thermal regimes (see section 5.2). With respect to other rock-type tor sites with complex exposure histories, we conclude that, in general, granite and schist tors (Raab et al., 2021) are equally suited for this approach.

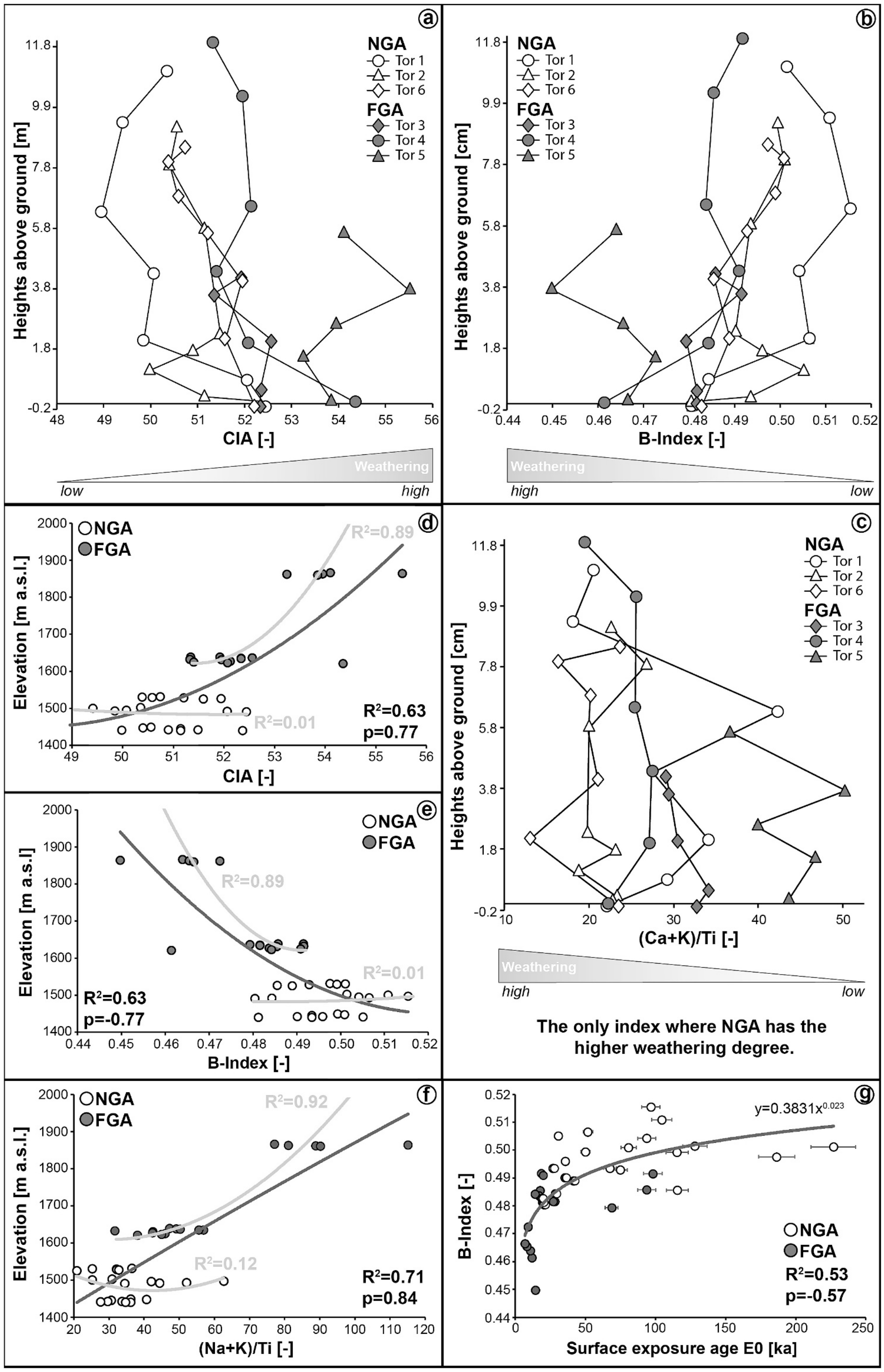

Fig. 8. Plots of tor (rock) weathering relation of sample height to (a) the chemical index of alteration (CIA) (Nesbitt and Young, 1982), (b) the B-index (Kronberg and Nesbitt, 1981) and (c) the (Ca + K)/Ti ratio. (d), (e) and (f) present the relation of the named weathering indices and the elevation above sea level (a.s.l.) (g) Calculated surface exposure ages plotted against the selected B-index. Further indices are found in Table S4.

5.2. Isotope signatures and glacial links of tors (Hypotheses II and III)

At the Serra da Estrela, glacial erosion occurred mainly near the plateau margins and valley heads and along the main valley's axes (Vieira, 2008). During the LGMSE, the Vale do Conde (Fig. 1d) was approximately covered by 100 m of ice, but the sites of Tors 3 and 4 were covered by 11 to 15 m and 30 to 50 m of ice, respectively (Vieira, 2008). The basal thermal regime is, however, still debated. The 22.5 ± 2 ka old (Raab et al., 2022) moraine boulder of the boulder field, embedding Tor 3 and partially Tor 4, shows that the locality was, at one point, covered with (polythermal) ice. Thus, the three surface exposure ages of Tor 3 in FGA provide evidence for preservation of TCN signatures of tors (or transitions in roches moutonnées features) under the ice. This could relate either to low erosion under thin ice, or to polythermal ice, with

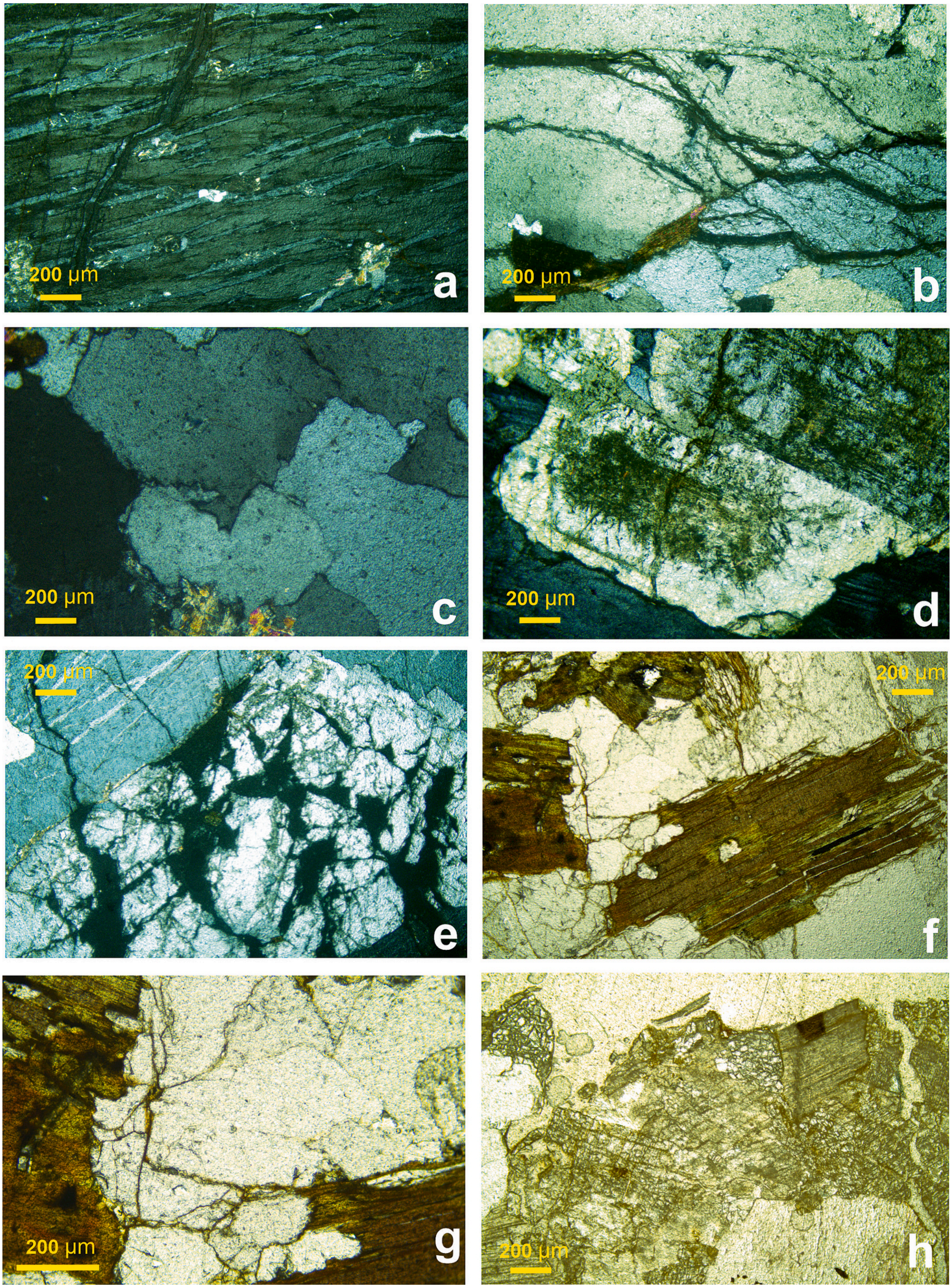

Fig. 9. Microphotographs of surface rock samples from the investigated tors in thin section. (a) Sheared feldspar with parallel wavy extinction and subparallel microcracks oriented along a different direction; cracks occasionally intersect and widen by chemical dissolution (Tor 1–5, XPL). (b) Polycrystalline quartz with wavy extinction; major cracks are subparallel and almost conformable to the rock surface (Tor 4–6, XPL). (c) Deformed quartz showing some scratches and weak dissolution features (Tor 2–1, XPL). (d) Zoned plagioclase (lower grain) affected by severe weathering in its core and intensely weathered feldspar (upper grain) with evidence of dissolution and clay neogenesis (Tor 1–2, XPL). (e) Plagioclase affected by cavernous weathering due to deep dissolution (Tor 1–5, XPL). (f) Different biotite grains (separated by quartz and a few feldspar crystals) display varying weathering degrees and features, such as flaking along cleavage planes, segregation of iron oxides, and neogenesis of clays, along with their migration into the surrounding microcracks (Tor 2–1, PPL). (g) Detail of the image reported in (f) at higher magnification. (h) Crossed to irregular, densely distributed microcracks affecting quartz, plagioclase, and feldspar near the rock surface (Tor 5–5, PPL). PPL: plane polarized light; XPL: crossed polarized light.

TABLE 3
Degree of weathering based on microscopic observations of rock thin sections from the investigated tors. Samples are ordered according to decreasing height above ground and corresponding exposure ages. Legend: -: null (not detected in the studied samples); [+]: very week (not detected in the studied samples); +: weak (not detected in the studied samples); ++: moderate; +++: high; ++++: very high; +++++: extremely high; (+): intermediate between two subsequent classes. NGA: non glaciated areas; FGA: formerly glaciated area.

Study area	Tor	Sample	Degree of weathering
NGA	Tor 1	Tor 1–2-Upper-Middle	+++
		Tor 1–5-Bottom	++
		Tor 1–6-Subsurface	+++(+)
NGA	Tor 2	Tor 2–1-Top	++++
		Tor 2–8-Between 4 and 5	+++(+)
		Tor 2–5-Bottom	++
		Tor 2–6-Subsurface	++++
FGA	Tor 3	Tor 3–1-Top	++++
		Tor 3–2-Upper-Middle	+++(+)
		Tor 3–1-Middle	++++
		Tor 3–1-Bottom	++++
FGA	Tor 4	Tor 4–1-Top	+++
		Tor 4–2-Upper-Middle	+++
		Tor 4–3-Middle	+++(+)
		Tor 4–6-Subsurface	++++
FGA	Tor 5	Tor 5–1-Top	+++
		Tor 5–2-Upper-Middle	+++(+)
		Tor 5–3-Middle	++++
		Tor 5–4-Lower-Middle	++++
		Tor 5–5-Bottom	++++
NGA	Tor 6	Tor 6–1-Top	+++
		Tor 6–7-Top2	+++
		Tor 6–2-Upper Middle	+++
		Tor 6–3-Middle	++++
		Tor 6–4-Lower Middle	++++
		Tor 6–5-Bottom	++++

warm ice advancing over a cold bed-frozen glacier. Previous findings of tors within glacial erratic and boulder fields (e.g., Sugden, 1968; Sugden and Watts, 1977) have indicated that the tors can indeed remain unchanged under cold-based and stationary ice (e.g., Kleman and Stroeven, 1997; Stroeven et al., 2002). The preservation of e.g., Tor 3, would therefore support such conditions, since plucking and boulder transportation by cold-based ice can also occur on mountain tops (e.g., Hughes et al., 2022). Further, the tors at FGA show, that, depending on tor morphology and the efficacy of glacial erosions' efficacy, the physical remains of tors (e.g., André, 2004) and also the tors TCN-signatures can be preserved completely (Tor 3), partially (Tor 4) or being mainly lost (Tor 5). The near homogeneous TCN-content in vertical profiles of Tor 4 is considered to be the result of, e.g., (subglacial) chemical weathering (see section 5.3), glacial erosion and temporal cover of glacial till. The TCN profile of Tor 5 is considered to be the result of a potentially pre-interglacial hydrothermal weathering (see Fig. 8a, b) that was driven by its position within a major fault zone and the post-glacial mass wasting process.

Overall, the isotope signature trends (Fig. 4a) categorize the tors into two groups and differ between NGA and FGA sites. All NGA Tors 1, 2, 6, and Tor 3 in FGA have an increasing ^{10}Be content trend with heights above ground, supporting tor emergence through time, in response to regolith removal from the surroundings (Linton, 1955; Migoń, 2006). In contrast, FGA Tors 4 and 5 have a low and rather homogeneous ^{10}Be content along their vertical profiles, reflecting a relatively abrupt and faster exposure (~20–90 times) than NGA tors. The difference in exposure speed and surface exposure times of Tor 4 and 5 can be linked to the ice proximity (see also section 5.1), the post-LGM(SE) glacial retreat (Fig. 10a) and deglaciation (Fig. 10b) with elevation.

Considering that deglaciation starts at lower elevations first (Benn and Evans, 2014) and hypothesizing that the isotope clock of the rock surface was reset by glacial abrasion (near/full removal of TCN enriched minerals), we should see a decrease in the ^{10}Be content with higher elevations at FGA. This is precisely the case. The ^{10}Be content decreases with increasing elevation among FGA samples (Fig. 4b), reflecting a later tor surface exposure in the former accumulation zone (~1862 m; Tor 5) than at the glacier margin (~1635 m; Tor 4). In contrast, NGA tors confirm a ^{10}Be natural increase with elevation of past tor studies in non-glaciated areas (see summary of tor studies by Máčka et al., 2023) mainly because of the natural increase of TCN production rates with elevation (e.g., Gosse and Phillips, 2001).

Based on the timing and current understanding of local glacial dynamics, Tor 4 has experienced the removal of rock surfaces predominantly by glacial erosion, postglacial mass wasting (also of till cover) and/or prolonged direct shielding by ice, while Tor 5 was controlled by postglacial mass wasting of the highly weathered rock surface and the regolith.

By contrast, the Penhas Douradas plateau (NGA; Fig. 1c) has not experienced glacial modification of the landscape in the last ca. 200 ka and the ^{10}Be contents are therefore markedly higher. Among them, however, Tor 2 stands out by lower ^{10}Be contents, which is consistent with its geomorphic setting close to the plateau margin, within the rim of a minor basin evidently subject to faster erosion than the adjacent sites (Tors 1 and 6) on the proper plateau.

Past glacial extents and ice conditions can be indicated by various geomorphological features (e.g., boulders, erratics, roches moutonnées, plucking, etc.). We see tors, if available, as a complementary proxy to identify ice extents as assumed in previous studies (e.g., Phillips et al., 2006; Gunnell et al., 2013), because they are rooted in bedrock in contrast to ex-situ boulders. The age differences between Tor 3, Tor 4, and Boulder 1 (see also section 5.1) indicate the value of tor record. Within the marginal moraine complex at the Vale do Conde, Boulder 1 marks a maximum ice extent at 22.5 ± 2 ka and ~ 1638 [m a.s.l.]. Tor 3, exhibiting a surface exposure age of over 100 ka at ~1638 [m a.s.l.], within the moraine boulder field, puts direct ice flow at this location in question, suggesting that the Tor 3 site inside the boulder field could have been under polythermal ice, as shown in blockfield studies (e.g., Goehring et al., 2008). Moreover, Tor 3 illustrates that tors can survive glacial activity and are thus a valid environmental archive for formerly glaciated areas. Therefore, we reason that the glacial dynamics around Tor 3 were sufficient to form a scattered allochthonous boulder field, yet limited in the ability to erode above the valley slope knickpoint. A valley cross-section (Fig. 11) illustrates that Boulder 1 and Tor 3 are positioned at the knick-point to the glacial valley. No fresh glacial erosion marks are present in the area around Boulder 1 and Tor 3, although it is within the regional equilibrium line altitude (ELA) of about 1650 [m a.s.l.] (Vieira et al., 2021). Among the selected tors, the best evidence for deglaciation in the Vale do Conde (valley bottom at ~1590 [m a.s.l.]) is provided by Tor 4, suggesting 19 ± 1 ka at ~1632 [m a.s.l.] while 12 ± 1 ka at ~1620 [m a.s.l.] is a too young age, which suggests that most of the ages recorded in Tor 4 are exposure times after the erosion of a potential till cover. The suggested final deglaciation for the Serra da Estrela by Vieira et al. (2021) is during the Bølling-Allerød interstadial (14.6–12.9 ka) and its validity for areas in the elevation range of about 1400–1750 [m a.s.l.] can be supported by the Tor 4.

Tor 5 is located 131 m (at ~1862 m) below the highest point of the Serra da Estrela (Torre, 1993 m) and has a low isotope signature (Fig. 4a; Table 2) up to two metres from its base. The respective surface exposure ages of around 6 ± 0.5 ka (Fig. 5e) would coincide with the transition from a moist and cool to an oceanic-Mediterranean climate (Fig. 10c). The high chemical weathering degree paired with young and abrupt surface exposure support that the tor columns at the Covão do Boi (Tor 5) are the result of a postglacial mass wasting and precipitation-driven erosion as suggested by Ferreira and Vieira (1999). Thus, minerals altered during the prolonged time of deep weathering and saprolite formation have just been recently (~11–6 ka) exposed to the surface (Fig. 12a,b,c).

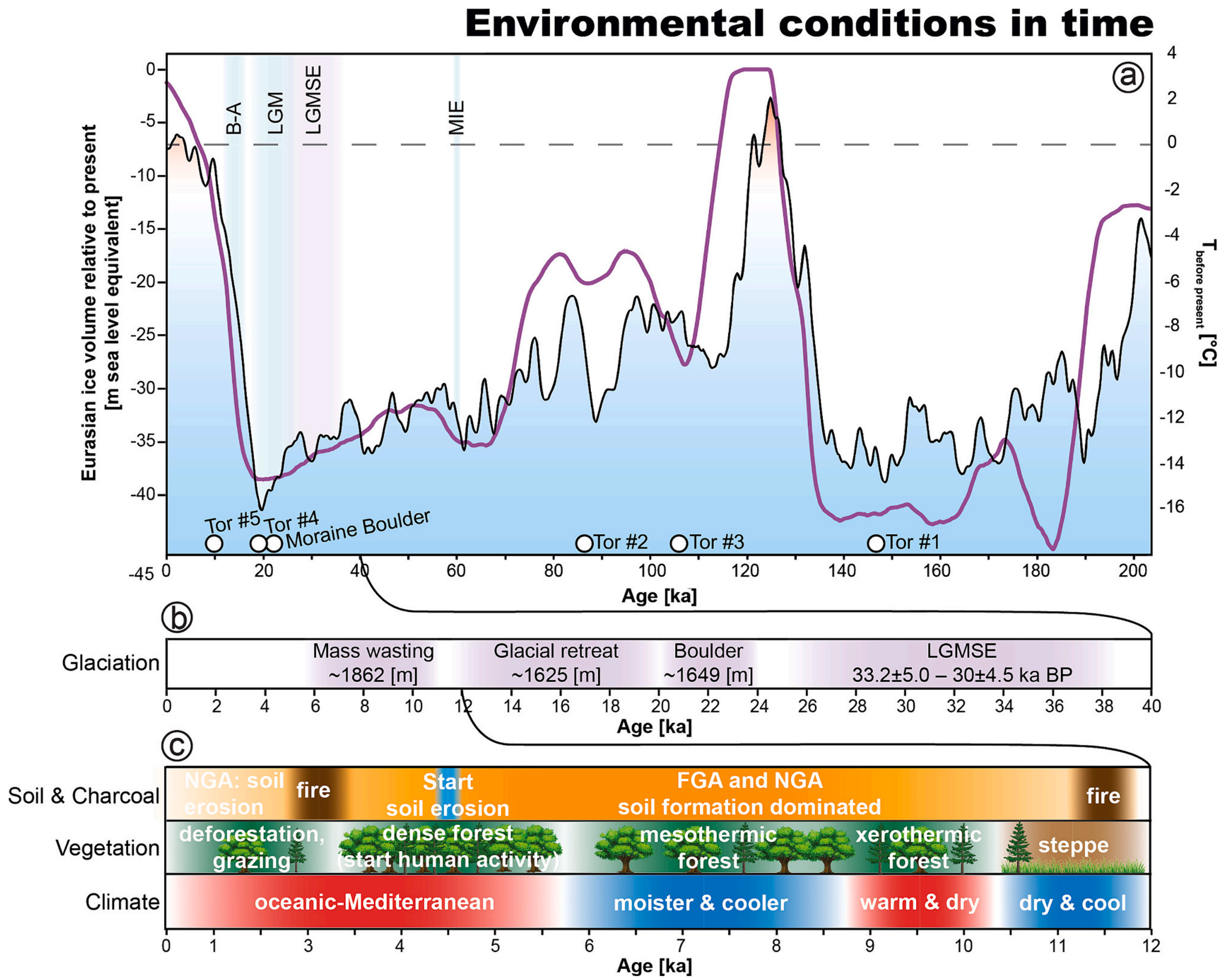

Fig. 10. (a) Earliest surface exposer of the investigated tors and boulder in context to the atmospheric surface air temperature and Eurasian ice volume relative to present after Bintanja et al. (2005). The Bølling-Allerød (B-A), Last Glacial Maxima (LGM), Last Glacial Maxima of the Serra da Estrela (LGMSE) and the Maximum Ice Extent (MIE) of the Pyrenees are indicated. (b) Short illustration of the glacial information for the last 40 ka for the Serra da Estrela. (c) Highlighting the environmental conditions of soil (Connor et al., 2012; Raab et al., 2022), vegetation and climate (van der Knaap et al., (1995).

5.3. *Chemical weathering patterns (Hypothesis IV)*

In general, the more time is available for weathering, the more rocks are transformed by dissolution, oxidation, hydrolysis, and mechanical destruction (Press et al., 2008). However, in the Serra da Estrela the signal obtained from chemical weathering indices is ambiguous. The (Ca + K)/Ti ratio indicates a higher weathering degree in NGA, whereas the CIA and B-index show the opposite (Fig. 8a,b,c). Overall, the weathering indices in the Serra da Estrela are lower compared to e.g., granite tors in Finland (CIA of 59; in-situ ^{10}Be ages of 55.8 ± 4.5 to 89.1 ± 6.7 ka; Darmody et al., 2008) and opposite to the weathering pattern found in the local soil (Raab et al., 2022). Yet the weathering degree of the topsoils in NGA (B-index: ~0.40, CIA: ~70) and FGA (B-index: ~0.40, CIA: ~60) (Raab et al., 2022) correspond to the expected continuous weathering of minerals with time. In the relatively flat (to moderately inclined) area, we find the lowest chemical weathering degree (Tor 1, Fig. 8a,b), while tors in higher elevation settings show the highest values (e.g., Tor 5, Fig., 6a,b). Thus, we observe an additional opposite trend to ordinary chemical weathering patterns, when using the CIA or B-Index (Press et al., 2008). However, the (Ca + K)/Ti index resulted in a more expected weathering pattern, with longer exposed surfaces having a higher weathering severity. Yet, some individual tor weathering patterns (e.g., Tor 1, Tor 4, Fig. 8c) even overlap Hence, time, morphology, and rock type (all granite, with slight differences in mineral content and grain size) do not explain the weathering patterns in the Serra da Estrela. We consider hydrolysis, controlled by (melt) water availability and general subglacial weathering regimes (e.g., Graly et al., 2014) paired with post-glacial exhumation weathering, as key factors for the observed chemical weathering pattern.

A longer subglacial residence time and, thus, contact with water enhances silicate dissolution (Wadham et al., 2010). Tors having a longer contact with (melt)water or warm-based ice will undergo a more vigorous silicate decomposition due to hydrolysis (e.g., Tranter et al., 2002). Hence, in the proximity to a glacial terminus (Tor 4), (melt)water (see also section 5.1) could have leached the rock surfaces. We also consider polythermal and warm-based ice within the glacier accumulation zone (Tor 5) to have driven mechanical freeze-thaw weathering processes in microcracks that caused mineral alteration also during saprolite formation at depth (e.g., Watts, 1985). The fast, near abrupt exposure of Tor 5 (Fig. 7f) supports the link of strong chemical weathering (Fig. 8a,b) and the effective erosion rate documented in past studies (e.g., Anderson, 2005). Thus, although the surface ages of Tor 5 are the youngest among all tors (Fig. 5e), the weathering degree is the highest (Fig. 8a,b).

Thin-section microscopy of the samples shed some into the complex patterns of weathering of each tor. Obviously, the effects of physical

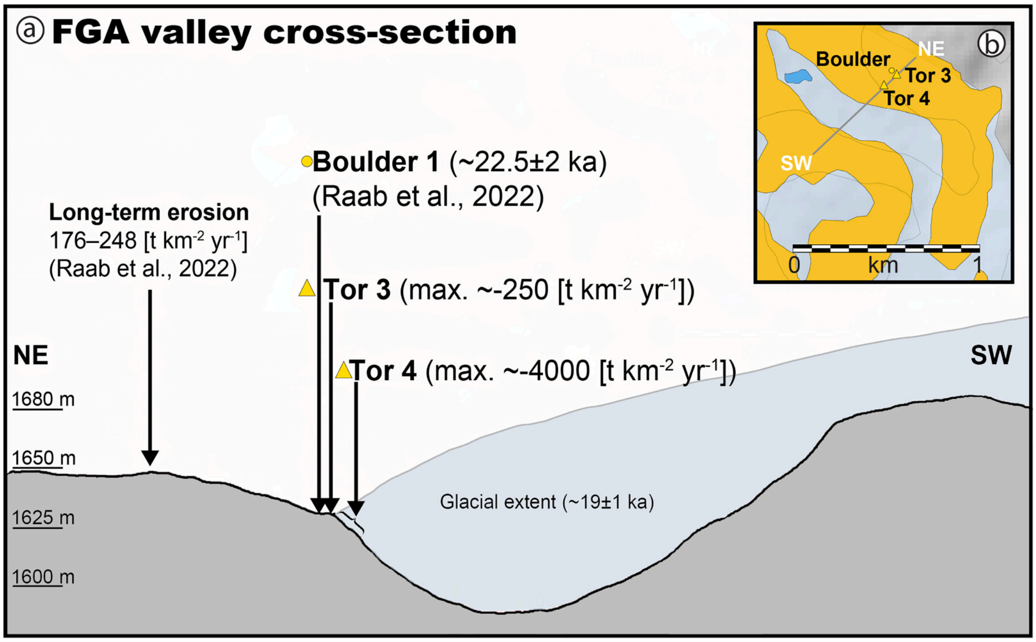

Fig. 11. (a) Detailed cross-section of the investigated formally glaciated area and location of long-term erosion rates after Raab et al. (2022). Potential glacial extent based on the surface ages (rock erosion of 1 [mm kyr^{-1}]) of Tor #4. (b) Orientation map specifying the position of the cross-section.

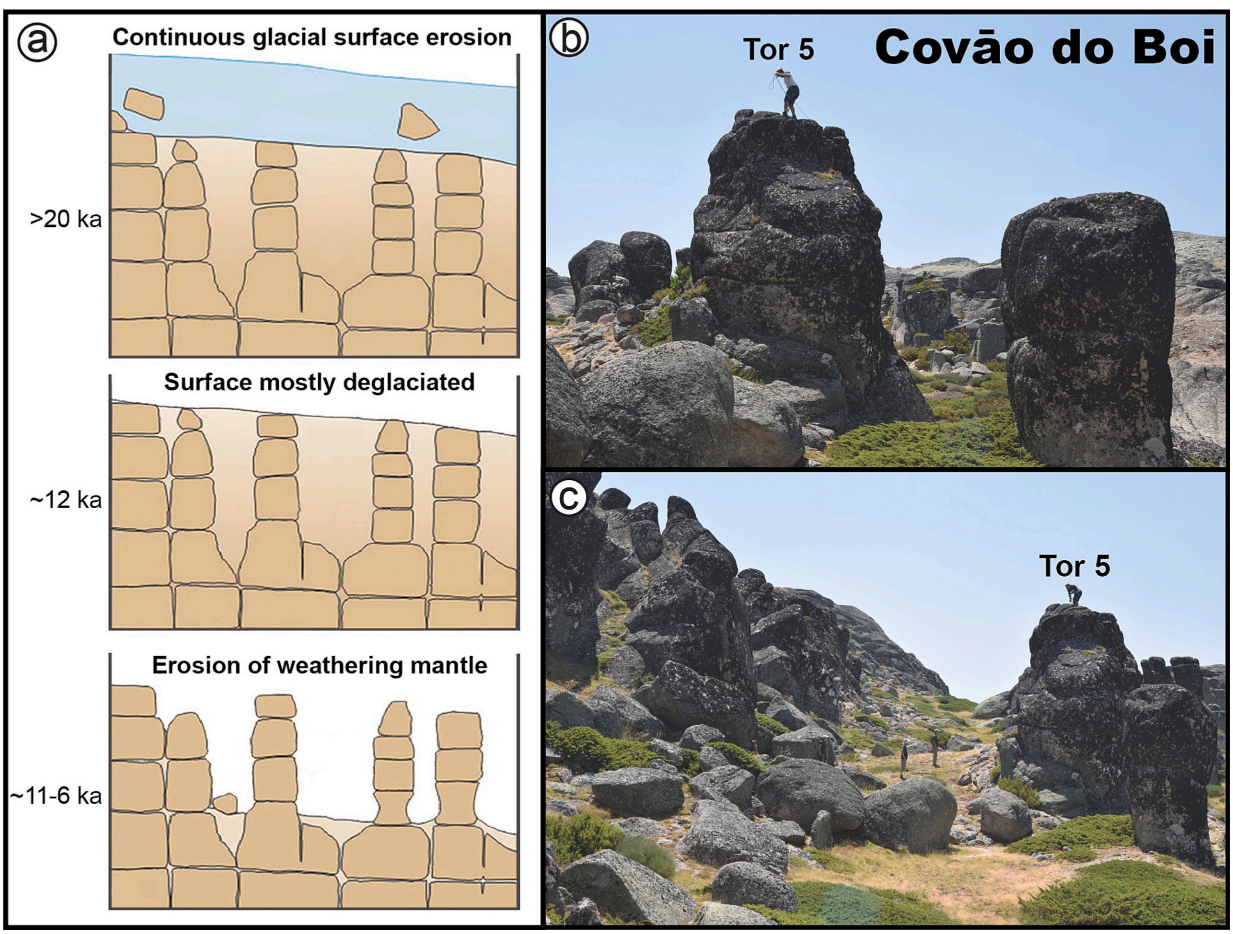

Fig. 12. (a) Evolution of the Covão do Boi (Tor 5; modified after Vieira et al., 2017)) area. Before surface exposure, the area was continuously reshaped by glacier abrasion and plucking. After the deglaciation of the Serra da Estrela, the future tor columns remained embedded in a weathering mantle with very strong mineral alteration (Fig. 6a,b demonstrate that Tor 5 has the highest weathering degree). In the last stage, the tors were exposed through a rapid (Fig. 5f) removal of the weathered material. (b), (c) Today, a series of these wonderfully-preserved tors remain.

weathering processes that led to surface rock cracking (presumably freeze-thaw and thermal fatigue dynamics; e.g., Scarciglia et al., 2022) are not recorded by the chemically-based alteration indices, which therefore underestimate the weathering severity (Scarciglia et al., 2016). Moreover, translocation of clays and Fe-oxides, due to percolating water through rock cracks, can cause an overestimation of in situ chemical weathering and create corresponding irregular depth-patterns where illuviation was more intense (Scarciglia et al., 2016). Time likely controlled further the weathering degree along the tors. Later exhumation stages that exposed the lower portions of the tors. This implies longer time of action of weathering and a corresponding increase in weathering severity. However, some weathering processes clearly acted before the onset of denudation, when the entire tor was still undergoing shaping (rounding) below-ground within the saprolite at depths where infiltrating water was present. Therefore, the severity of chemical weathering predominantly depends on the contact of water with rocks and time of exposure to water. During the initial topography lowering and the start of major physical degradation processes above ground, chemical weathering processes were still active underground, accompanying rejuvenation of the weathering front. The observed increasing weathering trend with increasing elevation (Fig. 8c,e,d) is symptomatic of such dynamics, mainly evident in element ratios using highly soluble cations (Fig. 8e) which have a higher correlation ($p = 0.84$) than weathering indices that include moderately soluble cations (Fig. 8c,d; $p = 0.77$). Based on oldest exposure ages of all the tors except Tor 4, it can be supposed that some chemical weathering processes occurred during the last interglacial at least, and not only during the last glaciation and subsequent deglaciation phases. Chemical weathering in Covão do Boi (Tor 5) may have occurred even before the last interglacial period, as the area is interpreted as a fault zone that could have created hydrothermal weathering conditions.

5.4. $D_{Surface}$ patterns and rates (Hypothesis V)

Different $D_{Surface}$ patterns were identified among the investigated tors. Tors 4 and 5, both positioned within FGA, show similar trends (see section 5.2), as do Tors 1 and 3 (Fig. 13). Conversely, Tors 2 and 6 do not show similarities to any of the above. The formerly glaciated tors (Tor 4, Tor 5) have the highest $D_{Surface}$ among all investigated tors. The $D_{Surface}$ derived maxima from the glaciated tors (~18 [mm yr^{-1}]; Tor 5, Tor 4) are 20 to 360 times higher than obtained for tors in previous studies, at plateau summits in New Zealand (0.03–0.22 [mm yr^{-1}], Raab et al., 2021), Australia (0.007–0.016 [mm yr^{-1}], Heimsath et al., 2001a), Sweden (<0.02 [mm yr^{-1}], Stroeven et al., 2002) or Scotland (~0.045–0.09 [mm yr^{-1}], Phillips et al., 2006). We understand that these extreme $D_{Surface}$ maxima at the Serra da Estrela reflect glacial erosion or removal of glacial debris impact on the landscape as well as tor degradation rates driven by subglacial weathering (see section 5.2) tor degradation rates as found in the other tor studies. As evident in our Tor 5 model (Fig. 7f), the removal of the saprolite must have been a rather abrupt (within 4 ka) transformation process. Yet, even the exclusion of Tor 5 leaves us with a staggering maximum $D_{Surface}$ rate of nearly 3 [mm yr^{-1}] (Tor 4), which is again 10–100 times higher than found in previous studies (see above). Thus, depending on the degree of glacial erosion on the tor archive, the derived $D_{Surface}$ rates can reflect the glacial period impact or the general long-term landscape evolution.

Tor 1 and Tor 3 have similar exposure trends. Starting at around 100 ka with a $D_{Surface}$ rate of ~0.12–0.15 [mm yr^{-1}], the rate decreases and reaches the lowest values during the LGMSE before increasing again to up to 0.25 [mm yr^{-1}]. The $D_{Surface}$ trend of Tor 3 presents a weak burial phase (~ −0.015 [mm yr^{-1}]) during the LGMSE in contrast to Tor 1 reaching a near-equilibrium between sedimentation and erosion, as the modelled negative erosion rates suggest. To consider these modelled rates a burial phase, additional TCNs (e.g., ^{26}Al, ^{14}C) must be measured within the same quartz sample. So far, we can only speculate that the negative erosion rates of Tor 3 result from the dynamics of the glacial ice (non-)activity in the Vale do Conde. Deposition of boulders and debris along the slope, frost wedging or stationary polythermal ice could explain the decrease of $D_{Surface}$ during the LGMSE. We tend to consider the latter as more plausible as other tor-rich relict landscapes have similar characteristics (e.g., Stroeven et al., 2002) and permafrost has been shown to be present in the Serra da Estrela at least during the coldest stages of the last glacial above ca. 1300 m a.s.l. (Nieuwendam et al., 2020). The evidence for the presence of the marginal moraine beyond the position of Tor 3 and no signs of bedrock erosion further suggest such an ice dynamic.

In general, the non-glaciated tors have a ~ 20–90-fold lower $D_{Surface}$ rate compared to the glaciated tors. Yet, the non-glaciated tors uncover a ~ 10-times longer $D_{Surface}$ history that agrees with the long-term (soil) erosion rates documented by Raab et al. (2022) (see comparison in Fig. 11a). The $D_{Surface}$ trends in the Serra da Estrela correspond to the patterns in the Sila massif (Italy) (Raab et al., 2018, 2019). First, at both sites, tors located at the summit position have a continuous increase in $D_{Surface}$ to ~0.14 [mm yr^{-1}] since their time of first exposure. Second, tors at/near slopes have a higher $D_{Surface}$ with similar maxima at both sites, Sila: ~0.30 [mm yr^{-1}] and Estrela: 0.25 [mm yr^{-1}]. Third, Sila tors near basins have a lower $D_{Surface}$ than the tors along slopes, as does Tor 2 in a small and narrow valley in a rugged relief sector of the Serra da

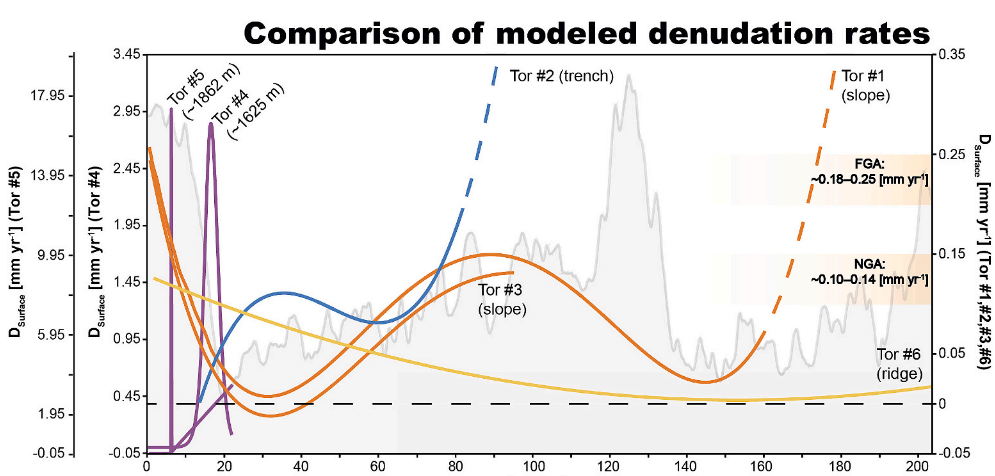

Fig. 13. Comparing the surface denudation averages with the average erosion rates for NGA and FGA after Raab et al. (2022) (orange rectangles only indicate the rates) A colour grouping of the $D_{Surface}$ rates is based on the exposition across the landscape. The backdrop presents the atmospheric surface air temperature after Bintanja et al. (2005) and serves as a reference to Fig. 7a.

Estrela. The peculiarly positioned Tor 2 (~1440 m) has an opposite $D_{Surface}$ trend compared to the slope tors (Fig. 13), peaking around the LGMSE when slope erosion was the lowest in Tors 1 and 3. Geomorphic evidence and the occurrence of remnant grus suggest that the valley was a weathering pocket. The resulting near opposite $D_{Surface}$ trend at Tor 2 with respect to Tors 1 and 3 (Fi.9) is probably the result of saprolite removal in the former. The modelled rapid $D_{Surface}$ decrease of Tor 2 during post-LGMSE is likely the expression of reduced efficacy of mass wasting process after saprolite was removed (similar to Tor 5).

5.5. Environmental conditions and $D_{Surface}$ variations (Hypothesis VI)

The tor exposure is linked to continuous erosion of the surrounding weathering mantle and overlying deposits, which, however, occurred with varying intensity. Most of tor top surface exposure ages (e.g., Tor 1: ~146 ka, Tor 2: 88 ka, Tor 3: ~103 ka) coincide with the period of lower temperatures when the Eurasian ice volume increased (negative sea level Fig. 10a). During the transition from the cool Late Pleistocene to the warmer Holocene, $D_{Surface}$ increased in both areas, indicated by Tor 1 (NGA) and Tor 3 (FGA) (Fig. 13).

Regarding $D_{Surface}$, Tor 1 and Tor 3 have parallel, near directly relational trends to the temperature variations (background in Fig. 13). During periods with low temperatures $D_{Surface}$ was low, whereas during periods with higher temperatures $D_{Surface}$ was high or comparatively increased. Yet, morphological controls on the tor archive, as discussed in section 5.3 for Tor 2 (valley) and Tor 6 (summit), appear to outweigh the impact of temperature controls (Fig. 13).

Tor 4 and Tor 5 located within FGA recorded the highest $D_{Surface}$ through the glacial retreat (see section 5.2) and postglacial mass-wasting respectively. The modelled $D_{Surface}$ peak of Tor 4 is around 16 ± 1 ka (Fig. 7d) fitting to the temperature rise (Fig. 10a; Fig. 9; Bintanja et al., 2005) before the Bølling-Allerød (14.69—12.89 ka BP). At higher elevations, the Tor 5 $D_{Surface}$ peak (~6 ± 0.5 ka) seems to reflect the transition from a moist and cool to an oceanic-Mediterranean climate (Fig. 10c; Van der Knaap and Van Leeuwen, 1995). After this climate transition, human activity (e.g., deforestation, grazing) started, accompanied by the onset of soil erosion around 4.55 ka BP (Fig. 10c; Connor et al., 2012). The coarse resolution of our models, however, hinders the identification of any links to the currently available vegetation history (e.g., Van der Knaap and Van Leeuwen, 1995) of the Serra da Estrela. Nevertheless, we can support the hypothesis that transitioning from a cooler to a warmer climate regime is linked to a rise in surface denudation.

5.6. Global applicability of the TEA

The genesis of tors is a complex process involving various geological mechanisms and weathering processes, yet with two principal basic steps. First, weathering selectively weakens parts of the bedrock, whereas and in the second step, the weakened material is removed while more resistant material parts remain emerged as standing tors. Thus, selective weathering and differential erosion are two major factors, although further weathering after exposure will reduce the tor and may ultimately lead to its complete degradation. Consequently, as long as the overall tor structure remains intact, the basic assumption of a gradual surface exposure required for the TEA, applies at all intact tor sites. This has been shown on multiple occasions (see above e.g., Heimsath et al., 2001a).

Of course, the dominating local processes impact the overall formation time and shape of tor sites, providing a landscape-formation-dependent variability. For example, the Serra da Estrela is sprinkled with corestone-like boulders on top of tors. The soil profiles along road sites, displaying still preserved corestone weathering patterns, point to the subsurface spheroidal weathering as the dominant mechanism in the area. However, at higher elevations, our impression is that fewer boulders/corestones are found on top of tors or outcrops (except for moraine fields). Thus, one could argue that in more elevated parts of the Serra da Estrela, joint spacing is a dominant control, and periglacial stripping played a major role (e.g., Palmer and Neilson, 1962), also with respect to mineralogical differences of local granites (e.g., Migoń and Vieira, 2014).

Nevertheless, the basic principle of selective weathering, in one form (e.g., simple chemical dissolution) or via multiple weathering mechanics (e.g., abrasion, freeze-thaw, thermal expansion, salt, exfoliation, glacial soil stripping, etc.) followed and accompanied by differential erosion unites all tor landscapes (at least at one point in time). Then, tor degradation may proceed involving various mechanisms, from granular disintegration to major collapses along opening joints, depending on rock characteristics and specific geomorphic/topographic setting. Thus, although tors at the Serra da Estrela have formed (probably) to some degree differently than tors in other areas, the underlying process that causes tors to be exposed to the surface remains denudation. Therefore, the TEA remains applicable as long as the sites for sampling are carefully selected. Careful selection is expressed by understanding the TCN production mechanics and geomorphic surface processes. For example, one should exclude sampling along a recent rock break-off since the TCN signal will be distorted (younger), and collapsed tors (e.g., Lundy, England; Rolfe et al., 2012) are unlikely to be suitable for the TEA.

Our study has demonstrated that thoughtful selection does enable the derivation of long-term surface denudation variations from tors, even in formerly glaciated landscapes. We think that the TEA can evolve into a broadly used tool to determine surface denudation variability and not just for a granite environment. Although tors are more common in granitic landscapes because they more efficiently resisting weathering after emergence and have joints that permit water to widen, deepen and smooth them, creating weathering pockets and thus starting a selective weathering process, there are still other rock-type tors. Past studies have already demonstrated the applicability on schist tors in New Zealand (Raab et al., 2021), opening the doors to investigate also other schist tor sites e.g., the Cordillera Pelada paleoplain (Chile). Further, it would be desirable to explore the TEA on limestone tors (e.g., Calcareous Alps, Austria), sandstone tors (e.g., Bohemian Massif, Czech Republic) or even basalt rock pinnacles (e.g., Azores), since the isotopic tools even for quartz poor rocks (e.g., ^{36}Cl, ^{3}He) are already available.

6. Conclusions

A characterisation of tor exposure histories in formerly glaciated and non-glaciated areas in the Serra da Estrela (Portugal) was performed. We discovered increasing surface exposure ages with tor heights up to ~200 ka. The measured ^{10}Be isotope contents of the tors increased with elevation in the non-glaciated area and decreased with elevation in the formerly glaciated area. The much younger time ranges reflects the deglaciation timeline starting at the Vale do Conde terminus (~1625 m; ~19 ± 1 ka) and ending with the mass wasting process in the Covão do Boi (~1862 m; ~6 ± 0.5 ka). Tors in the Vale do Conde captured glacial dynamics in more detail and also postglacial denudation. The resulting weathering indices and the TEA data support the postglacial mass wasting processes at the Covão do Boi, which was enabled by multi-millennial (hydrothermal) chemical weathering within a fault zone. The modelled surface denudation ranges from −0.04 to 0.53 [mm yr^{-1}] in the non-glaciated area and from −0.02 to 18.29 [mm yr^{-1}] in the formerly glaciated area. Besides the exceptionally high rates obtained from the formerly glaciated tors, surface denudation rates match the long-term soil erosion rates documented in previous studies (Raab et al., 2022). A direct relationship between temperature and surface denudation is indicated, as model averages were low during climate stages of low temperatures and increased during warmer conditions. Surface denudation has risen to new highs since the LGM. The final mass wasting stage was most likely initiated during the transition from a moist and cool to an oceanic Mediterranean climate. Morphological controls dictated by the position of the investigated tors have partially overshadowed the impact of temperature on erosion. However, the impact of vegetation changes or human activity on surface denudation remains unanswered due to the too low chronological resolution. Overall, the Tor Exhumation/Exposure Approach (TEA) has delivered virtually continuous in-situ surface denudation histories of the formerly glaciated areas and thus proved to be a promising universal tool for future geomorphological studies.

Supplementary data to this article can be found online at https://doi.org/10.1016/j.geomorph.2024.109416.

CRediT authorship contribution statement

Gerald Raab: Writing – review & editing, Writing – original draft, Visualization, Project administration, Methodology, Investigation, Funding acquisition, Formal analysis, Data curation, Conceptualization. **Gonçalo Vieira:** Writing – review & editing, Writing – original draft, Visualization, Methodology, Investigation, Data curation. **Piotr Migoń:** Writing – review & editing, Writing – original draft, Visualization, Investigation, Data curation. **Dmitry Tikhomirov:** Writing – review & editing, Writing – original draft, Methodology, Investigation. **Marcus Christl:** Writing – review & editing, Methodology, Investigation, Data curation. **Markus Egli:** Writing – review & editing, Writing – original draft, Methodology, Investigation, Data curation, Conceptualization. **Fabio Scarciglia:** Writing – review & editing, Writing – original draft, Visualization, Methodology, Investigation, Formal analysis, Data curation.

Declaration of competing interest

The authors declare that they have no known competing financial interests or personal relationships that could have appeared to influence the work reported in this paper.

Data availability

Supplementary files include raw data of sample measurements. Please get in touch with www.geraldraab.com for inquiries related to modelling and measurements. Detailed 3D drone models for individual tors are found on sketchfab.com. Please get in touch with Gonçalo Vieira for any drone-related inquiries. The entire drone data is freely available on Zenodo.

Acknowledgment

This research was supported by the Forschungskredit of the University of Zürich FK-19-108. Additional funds were provided by the Stiftung für Wissenschaftliche Forschung of the University of Zürich, grant no. STWF-20-02. Gerald Raab was supported by the Early Postdoc. Mobility Fellowship P2ZHP2_199662, of the Swiss National Science Foundation (SNSF). The Estrela UNESCO Global Geopark is thanked for logistical support to fieldwork especially Fábio Loureiro that worked hard with rock sampling. The Instituto da Conservação da Natureza e Florestas is thanked for granting the sampling and field work permits. Furthermore, we thank Helena Azeredo and her son for finding and returning one of our field books that got lost in Penhas Douradas. Lastly, we appreciate the critical comments of two anonymous reviewers and the editor, Markus Stoffel.

References

Anderson, S.P., 2005. Glaciers show direct linkage between erosion rate and chemical weathering fluxes. Geomorphology 67 (1–2), 147–157.

André, M.F., 2004. The geomorphic impact of glaciers as indicated by tors in North Sweden (Aurivaara, 68 N). Geomorphology 57 (3–4), 403–421.

Balco, G., 2017. The Online Exposure Age Calculator Formerly Known as the CRONUS-Earth Online Exposure Age Calculator.

Balco, G., Stone, J.O., Lifton, N.A., Dunai, T.J., 2008. A complete and easily accessible means of calculating surface exposure ages or erosion rates from 10Be and 26Al measurements. Quaternary Geochronology 8, 174–195. https://doi.org/10.1016/j.quageo.2007.12.001.

Ballantyne, C.K., 2018. Periglacial Geomorphology. Wiley Blackwell, Chichester, p. 454.

Beckhoff, B., Kanngießer, B., Langhoff, N., Wedell, R., Wolff, H., 2006. Handbook of Practical X-Ray Fluorescence Analysis. Springer, Berlin.

Benn, D., Evans, D.J., 2014. Glaciers and Glaciation. Routledge.

Benson, A., Hoffmann, D.L., Daura, J., Sanz, M., Rodrigues, F., Souto, P., Zilhão, J., 2021. A speleothem record from Portugal reveals phases of increased winter precipitation in western Iberia during the Holocene. The Holocene 31, 1–12. https://doi.org/10.1177/09596836211011666.

Bintanja, R., Van De Wal, R.S., Oerlemans, J., 2005. Modelled atmospheric temperatures and global sea levels over the past million years. Nature 437 (7055), 125–128.

Brown, E.T., Edmond, J.M., Raisbeck, G.M., Yiou, F., Desgarceaux, S., 1992. Effective attenuation length of cosmic rays producing ^{10}Be and ^{26}Al in quartz: Implications for surface exposure dating. Geophysi- cal Research Letters 9, 369–372. https://doi.org/10.1029/92GL00266.

Chmeleff, J., von Blanckenburg, F., Kossert, K., Jakob, D., 2010. Determination of the 10Be half-life by multicollector ICP-MS and liquid scintillation counting. Nuclear Instruments and Methods in Physics Research Section B: Beam Interactions with Materials and Atoms 268 (2), 192–199.

Christl, M., Vockenhguber, C., Kubik, P.Q., Wacker, L., Lachner, J., Alfimov, V., Synal, H. A., 2013. The ETH Zurich AMS facilities: Performance parameters and reference materials. Nucl. Inst. Methods Phys. Res. B 294, 29–38. https://doi.org/10.1016/j.nimb.2012.03.004.

Clark, P.U., 2009. The last Glacial Maximum. Science 325, 710–714.

Connor, S.E., Araújo, J., van der Knaap, W.O., van Leeuwen, J.F., 2012. A long-term perspective on biomass burning in the Serra da Estrela, Portugal. Quat. Sci. Rev. 55, 114–124.

Darmody, R.G., Thorn, C.E., Seppälä, M., Campbell, S.W., Li, Y.K., Harbor, J., 2008. Age and weathering status of granite tors in Arctic Finland (~ 68 N). Geomorphology 94 (1–2), 10–23.

Daveau, S., 1971. La glaciation de la Serra da Estrela. Finisterra 6, 5–40.

Domínguez-Villar, D., Razola, L., Carrasco, R.M., Jennings, C.E., Pedraza, J., 2009. Weathering phases recorded by gnammas developed since last glaciation at Serra da Estrela. Portugal. Quaternary Research 72 (2), 218–228.

Einsele, G., Hinderer, M., 1998. Quantifying denudation and sediment–accumulation systems (open and closed lakes): basic concepts and first results. Palaeogeogr. Palaeoclimatol. Palaeoecol. 140 (1–4), 7–21.

Ferreira, N., Vieira, G., 1999. Guia geológico e geomorfológico do Parque Natural da Serra da Estrela. Instituto Geológico e Mineiro, Parque Natural da Serra da Estrela, ICN, Ministério da Economia, p. 111.

Goehring, B.M., Brook, E.J., Linge, H., Raisbeck, G.M., a. Yiou, F., 2008. Beryllium-10 exposure ages of erratic boulders in southern Norway and implications for the history of the Fennoscandian ice sheet. Quaternary Science Reviews 27, 320–336.

Gonzalez, V.S., Bierman, P.R., Nichols, K.K., Rood, D.H., 2016. Long-term erosion rates of Panamanian drainage basins determined using in situ 10Be. Geomorphology 275, 1–15.

Gosse, J.C., Phillips, F.M., 2001. Terrestrial in situ produced cosmo- genic nuclides: Theory and application. Quaternary Science Reviews 20, 1475–1560. https://doi.org/10.1016/S0277-3791(00)00171-2.

Graly, J.A., Humphrey, N.F., Landowski, C.M., Harper, J.T., 2014. Chemical weathering under the Greenland ice sheet. Geology 42 (6), 551–554.

Gunnell, Y., Jarman, D., Braucher, R., Calvet, M., Delmas, M., Leanni, L., Bourles, D., Arnold, M., Aumaitre, G., Keddaouche, K., 2013. The granite tors of Dartmoor, Southwest England: rapid and recent emergence revealed by late Pleistocene cosmogenic apparent exposure ages. Quaternary Science Reviews 61, 62–76.

Hall, K., Thorn, C., Sumner, P., 2012. On the persistence of 'weathering'. Geomorphology 149–150, 1–10.

Heimsath, A.M., Chappell, J., Dietrich, W.E., Nishiizumi, K., Finkel, R.C., 2001a. Late Quaternary erosion in southeastern Australia: a field example using cosmogenic nuclides. Quat. Int. 83, 169–185.

Heimsath, A.M., Dietrich, W.E., Nishiizumi, K., Finkel, R.C., 2001b. Stochastic processes of soil production and transport: erosion rates, topographic variation and cosmogenic nuclides in the Oregon coast range. Earth Surf. Process. Landf. 26, 531–552.

Heimsath, A.M., DiBiase, R.A., Whipple, K.X., 2012. Soil production limits and the transition to bedrock-dominated landscapes. Nature 5, 210–214.

Hinderer, M., Kastowski, M., Kamelger, A., Bartolini, C., Schlunegger, F., 2013. River loads and modern denudation of the Alps—a review. Earth Sci. Rev. 118, 11–44.

Hughes, P.D., Gibbard, P.L., 2015. A stratigraphical basis for the last Glacial Maximum (LGM). Quat. Inte. 383, 174–185.

Hughes, P.D., Glasser, N.F., Fink, D., 2022. 10Be and 26Al exposure history of the highest mountains in Wales: evidence from Yr Wyddfa (Snowdon) and Y Glyderau for a nunatak landscape at the global last Glacial Maximum. Quaternary Science Reviews 286, 107523.

Kirchner, J.W., Finkel, R.C., Riebe, C.S., Granger, D.E., Clayton, J.L., King, J.G., Megahan, W.F., 2001. Mountain erosion over 10 yr, 10 ky, and 10 my time scales. Geology 29 (7), 591–594.

Kleman, J., Stroeven, A.P., 1997. Preglacial surface remnants and Quaternary glacial regimes in northwestern Sweden. Geomorphology 19 (1–2), 35–54.

Kohl, C., Nishiizumi, K., 1992. Chemical isolation of quartz for measure- ment of in-situ-produced cosmogenic nuclides. Geochimica Cosmochimica Acta 56, 3583–3587. https://doi.org/10.1016/0016- 7037(92)90401-4.

Korschinek, G., Bergmaier, A., Faestermann, T., Gerstmann, U.C., Remmert, A., 2010. A new value for the half-life of 10Be by heavy- ion elastic recoil detection and liquid scintillation counting. Nuclear Instruments and Methods in Physics Research Section B: Bean Interaction with Materials and Atoms 268, 187–191. https://doi.org/10.1016/j. nimb.2009.09.020.
Kronberg, G.I., Nesbitt, H.W., 1981. Quantification of weathering of soil chemistry and soil fertility. J. Soil Sci. 32, 453–459.
Kubik, P.W., Chrisl, M., 2010. ^{10}Be and ^{26}Al measurements at the Zurich 6 MV Tandem AMS facility. Nuclear Instruments and Methods B 268, 880–883. https://doi.org/10.1016/j.nimb.2009.10.054.
Larsen, I.J., Montgomery, D.R., Greenberg, H.M., 2014. The contribution of mountains to global denudation. Geology 42 (6), 527–530.
Lautensach, H., 1929. Eiszeitstudien in der Serra da Estrela (Portugal). Zeitschrift für Gletscherkunde 17, 324–369.
Lichter, J., 1998. Rates of weathering and chemical depletion in soils across a chronosequence of Lake Michigan sand dunes. Geoderma 85, 255–282. https://doi.org/https://doi.org/10.1016/S0016-7061(98)00026-3.
Lifton, N., Sato, T., Dunai, T.J., 2014. Scaling in situ cosmogenic nuclide production rates using analytical approximations to atmospheric cosmic-ray fluxes. Earth Planet. Sci. Lett. 386, 149–160.
Linton, D.L., 1955. The problem of tors. Geogr. J. 121 (4), 470–487.
Máčka, Z., Braucher, R., Migoń, P., Belova, O., Leichmann, J., ASTER Team, 2023. Gneissic tors in the central European upland: complex late Pleistocene forms? Geomorphology 108764.
Masarik, J., Frank, M., Schäfer, J.M., Wieler, R., 2001. Correction of in situ cosmogenic nuclide production rates for geomagnetic field intensity variations during the past 800,000 years. Geochim. Cosmochim. Acta 65 (17), 2995–3003.
Maxeiner, S., Synal, H.A., Christl, M., Suter, M., Müller, A., Vockenhuber, C., 2019. Proof-of-principle of a compact 300 kV multi-isotope AMS facility. Nucl. Instrum. Methods Phys. Res., Sect. B 439, 84–89. https://doi.org/10.1016/j.nimb.2018.11.028.
Meade, R.H., 1988. Movement and storage of sediment in river systems. In: Lerman, A., Meybeck, M. (Eds.), Physical and Chemical Weathering in Geochemical Cycles. Kluwer Academic Publishers, Dordrecht, Netherlands, pp. 165–179.
Migoń, P., 2006. Granite Landscapes of the World. OUP Oxford.
Migoń, P., Vieira, G., 2014. Granite geomorphology and its geological controls, Serra da Estrela, Portugal. Geomorphology 226, 1–14.
Moreno, J., Ramos, A.M., Raposeiro, P.M., Santos, R.N., Rodrigues, T., Naughton, F., Moreno, F., Trigo, R.M., Ibañez-Insa, J., Ludwig, P., Shi, X., Hernández, A., 2023. Identifying imprints of externally derived dust and halogens in the sedimentary record of an Iberian alpine Lake for the past~ 13,500 years–Lake Peixão, Serra da Estrela (Central Portugal). Sci. Total Environ. 903, 166179.
Mourier, B., Poulenard, J., Carcaillet, C., Williamson, D., 2010. Soil evolution and subalpine ecosystem changes in the French Alps inferred from geochemical analysis of lacustrine sediments. J. Paleolimnol. 44 (2), 571–587.
Nesbitt, H.W., Young, G.M., 1982. Early Proterozoic climates and plate motions inferred from major element chemistry of lutites. Nature 299, 715–717.
Nieuwendam, A., Vieira, G., Schaefer, C., Woronko, B., Johansson, M., 2020. Reconstructing cold climate paleoenvironments from micromorphological analysis of relict slope deposits (Serra da Estrela, Central Portugal). Permafrost and Periglacial Processes 31 (4), 567–586. https://doi.org/10.1002/ppp.2054.
Nishiizumi, K., Imamura, M., Caffee, M.W., Southon, J.R., Finkel, R.C., McAnich, J., 2007. Absolute calibration of ^{10}Be AMS standards. Nuclear Instruments Methods in Physics Research Section B-Beam Inter- actions with Materials and Atoms 258, 403–413. https://doi.org/10.1016/j.nimb.2007.01.297.
Norton, K.P., von Blanckenburg, F., Kubik, P.W., 2010. Cosmogenic nuclide-derived rates of diffusive and episodic erosion in the glacially sculpted upper Rhone Valley, Swiss Alps. Earth Surf. Process. Landf. 35, 651–662.
Oliva, M., Palacios, D., Fernández-Fernández, J.M., Rodríguez-Rodríguez, L., García-Ruiz, J.M., Andrés, N., Carrasco, R.M., Pedraza, J., Pérez-Alberti, A., Valcárcel, M., Hughes, P.D., 2019. Late Quaternary glacial phases in the Iberian Peninsula. Earth Sci. Rev. 192, 564–600.
Palmer, J., Neilson, R.A., 1962. The origin of granite tors on Dartmoor, Devonshire. Proc. Yorks. Geol. Soc. 33 (3), 315–340.
Parker, A., 1970. An index of weathering for silicate rocks. Geol. Mag. 107 (6), 501–504.
Phillips, W.M., Hall, A.M., Mottram, R., Fifield, L.K., Sugden, D.E., 2006. Cosmogenic 10Be and 26Al exposure ages of tors and erratics, Cairngorm Mountains, Scotland: timescales for the development of a classic landscape of selective linear glacial erosion. Geomorphology 73 (3–4), 222–245.
Pigati, J.S., Lifton, N.A., 2004. Geomagnetic effects on time-integrated cosmogenic nuclide production with emphasis on in situ 14C and 10Be. Earth Planet. Sci. Lett. 226 (1–2), 193–205.
Press, F., Siever, R., Grotzinger, J.P., 2008. Allgemeine Geologie. Verlag, Spektrum, Akad.
Raab, G., 2019. The Tor Exhumation Approach – a New Technique to Derive Continuous In-Situ Soil Erosion and Surface Denudation Models. Dissertation. https://doi.org/10.13140/RG.2.2.29904.87043.
Raab, G., Scarciglia, F., Norton, K., Dahms, D., Brandová, D., de Castro Portes, R., Christl, M., Kletterer, M.E., Ruppli, A., Egli, M., 2018. Denudation variability of the Sila Massif upland (Italy) from decades to millennia using ^{10}Be and $^{239+240}$Pu. Land Degrad. Dev. 29, 3736–3752. https://doi.org/10.1002/ldr.3120.
Raab, G., Adam, P.M., Norton, K.P., Christl, M., Scarciglia, F., Egli, M., 2021. Complex patterns of schist tor exposure and surface uplift, Otago (New Zealand). Geomorphology 389. https://doi.org/10.1016/j.geomorph.2021. 107849.
Raab, G., Dollenmeier, W., Tikhomirov, D., Vieira, G., Migoń, P., Ketterer, M.E., Christl, M., Stutz, J., Egli, M., 2022. Contrasting soil dynamics in a formerly glaciated and non-glaciated Mediterranean mountain plateau (Serra da Estrela, Portugal). Catena 215. https://doi.org/10.1016/j.catena.2022.106314.
Rolfe, C.J., Hughes, P.D., Fenton, C.R., Schnabel, C., Xu, S., Brown, A.G., 2012. Paired 26Al and 10Be exposure ages from Lundy: new evidence for the extent and timing of Devensian glaciation in the southern British Isles. Quaternary Science Reviews 43, 61–73.
Saunders, I., Young, A., 1983. Rates of surface processes on slopes, slope retreat and denudation. Earth Surf. Process. Landf. 8 (5), 473–501.
Scarciglia, F., Critelli, S., Borrelli, L., Coniglio, S., Muto, F., Perri, F., 2016. Weathering profiles in granitoid rocks of the Sila Massif uplands, Calabria, southern Italy: new insights into their formation processes and rates. Sediment. Geol. 336, 46–67.
Scarciglia, F., Marsico, A., Capolongo, D., 2022. Weathering processes and rates of scarp retreat in a Mediterranean mountain environment: a multi-analytical approach from terrestrial laser scanning to microscale surveys. Geomorphology 413 (108356), 1–17.
Schaller, M., Ehlers, T.A., 2006. Limits to quantifying climate driven changes in denudation rates with cosmogenic radionuclides. Earth Planet. Sci. Lett. 248 (1–2), 153–167.
Schaller, M., von Blanckenburg, F., Hovius, N., Kubik, P.W., 2001. Large-scale erosion rates from in situ-produced cosmogenic nuclides in European river sediments. Earth Planet. Sci. Lett. 188 (3–4), 441–458.
Schaller, M., Blum, J.D., Ehlers, T.A., 2010. Combining cosmogenic nuclides and major elements from moraine soil profiles to improve weathering rate estimates. Geomorphology 15, 117–128.
Shuster, D.L., Cuffey, K.M., Sanders, J.W., Balco, G., 2011. Thermochronometry reveals headward propagation of erosion in an Alpine landscape. Science 332, 84–88.
Stock, J.D., Montgomery, D.R., 1999. Geologic constraints on bedrock river incision using the stream power law. J. Geophys. Res. 104, 4983–4993.
Stroeven, A.P., Fabel, D., Hättestrand, C., Harbor, J., 2002. A relict landscape in the Centre of Fennoscandian glaciation: cosmogenic radionuclide evidence of tors preserved through multiple glacial cycles. Geomorphology 44 (1–2), 145–154.
Sugden, D.E., 1968. The selectivity of glacial erosion in the Cairngorm Mountains, Scotland. Trans. Inst. Br. Geogr. 79–92.
Sugden, D.E., Watts, S.H., 1977. Tors, felsenmeer, and glaciation in northern Cumberland Peninsula, Baffin Island. Can. J. Earth Sci. 14 (12), 2817–2823.
Tikhomirov, D., Akçar, N., Ivy-Ochs, S., Alfimov, V., Schlüchter, C., 2014. Calculation of shielding factors for production of cosmogenic nuclides in fault scarps. Quat. Geochronol. 19, 181–193.
Tranter, M., Sharp, M.J., Lamb, H.R., Brown, G.H., Hubbard, B.P., Willis, I.C., 2002. Geochemical weathering at the bed of Haut Glacier d`Arolla, Switzerland—a new model. Hydrol. Process. 16 (5), 959–993.
Valla, P.G., Shuster, D.L., van der Beek, P.A., 2011. Significant increase in relief of the Eu- ropean Alps during mid-Pleistocene glaciations. Nat. Geosci. 4, 688–692.
Van Den Brink, L.M., Janssen, C.R., 1985. The effect of human activities during cultural phases on the development of montane vegetation in the Serra da Estrela. Portugal. Rev. Palaeobotany Palinol. 44, 193–205.
Van der Knaap, W.O., Van Leeuwen, J.F.N., 1995. Holocene vegetation succession and degradation as responses to climatic change and human activity in the Serra da Estrela. Portugal. Rev. Palaeobotany Palynol. 89, 153–211.
Van der Knaap, W.O., Van Leeuwen, J.F.N., 1997. Holocene vegetation successions, altitudinal vegetation zonation, and climatic change in the Serra da Estrela. Rev. Paleobot. Palynol 97, 239–285.
Vieira, G., 2004. Geomorfologia dos planaltos e altos vales da Serra da Estrela. Ambientes frios do Plistocénico Superior e dinâmica actual. PhD dissertation in Geography (Physical Geography),. University of Lisbon, Portugal.
Vieira, G., 2008. Combined numerical and geomorphological reconstruction of the Serra da Estrela plateau icefield. Portugal. Geomorphology 97 (1–2), 190–207.
Vieira, G.T., Ferreira, A. B. ,1998. General characteristics of the glacial geomorphology of the Serra da Estrela, in Vieira, G. T. (ed), Glacial and Periglacial Geomorphology of the Serra da Estrela. Guidebook for the field-trip, IGU Commission on Climate Change and Periglacial Environments, 26–28 August 1998, CEG and Department of Geography, University of Lisbon: 37–48.
Vieira, G., de Castro, E., Loureiro, F., Patrocinio, F., Firmino, G., Gomes, H., Fernandes, M., Forte, F., 2017. Application Dossier for UNESCO Global Geopark. Aspiring Geopark Estrela. November.
Vieira, G., Palacios, D., Andrés, N., Mora, C., Selem, L.V., Woronko, B., Soncco, C., Ubeda, J., Goyanes, G., 2021. Penultimate glacial cycle glacier extent in the Iberian Peninsula: new evidence from the Serra da Estrela (Central System, Portugal). Geomorphology 388, 107781.
Wadham, J.L., Tranter, M., Skidmore, M., Hodson, A.J., Priscu, J., Lyons, W.B., Sharp, M., Wynn, P., Jackson, M., 2010. Biogeochemical weathering under ice: size matters. Global Biogeochem. Cycles 24 (3).
Wallbrink, P.J., Murray, A.S., 1993. Use of fallout radionuclides as indicators of erosion processes. Hydrol. Process. 7 (3), 297–304.
Walling, D. E. (1998). Use of 137 Cs and other fallout radionuclide in soil erosion investigations: progress, problems and prospects (no. IAEA-TECDOC–1028).
Watts, S.H., 1985. A scanning electron microscope study of bedrock microfractures in granites under high arctic conditions. Earth Surf. Process. Landf. 10 (2), 161–172.
Wittmann, H., von Blanckenburg, F., Dannhaus, N., Bouchez, J., Gaillardet, J., Guyot, J. L., Christl, M., 2015. A test of the cosmogenic 10Be (meteoric)/9Be proxy for simultaneously determining basin-wide erosion rates, denudation rates, and the degree of weathering in the Amazon basin. J. Geophys. Res. Earth 120 (12), 2498–2528.